

The age of surface-exposed ice along the northern margin of the Greenland Ice Sheet

Joseph A. MacGregor ^{1*}, Mark A. Fahnestock ², William T. Colgan ³, Nicolaj K. Larsen ⁴, Kristian K. Kjeldsen ³ and Jeffrey M. Welker ^{5,6}

¹ Cryospheric Sciences Laboratory, NASA Goddard Space Flight Center, Greenbelt, Maryland, USA

² Geophysical Institute, University of Alaska Fairbanks, Fairbanks, Alaska, USA

³ Geological Survey of Denmark and Greenland, Copenhagen, Denmark

⁴ Section for GeoGenetics, Globe Institute, University of Copenhagen, Copenhagen, Denmark

⁵ Dept. of Biological Sciences, University of Alaska Anchorage, Anchorage, Alaska, USA

⁶ Dept. of Ecology and Genetics, University of Oulu, Oulu, Finland

* Corresponding author: Joseph A. MacGregor, Cryospheric Sciences Lab (Code 615), NASA Goddard Space Flight Center, 8800 Greenbelt Rd, Greenbelt, MD 20771, USA. Email: joseph.a.macgregor@nasa.gov.

Abstract

Each summer, surface melting of the margin of the Greenland Ice Sheet exposes a distinctive visible stratigraphy that is related to past variability in subaerial dust deposition across the accumulation zone and subsequent ice flow toward the margin. Here we map this surface stratigraphy along the northern margin of the ice sheet using mosaicked Sentinel-2 multispectral satellite imagery from the end of the 2019 melt season and finer-resolution WorldView-2/3 imagery for smaller regions of interest. We trace three distinct transitions in apparent dust concentration and the top of a darker basal layer. The three dust transitions have been identified previously as representing late-Pleistocene climatic transitions, allowing us to develop a coarse margin chronostratigraphy for northern Greenland. Substantial folding of late-Pleistocene stratigraphy is observed but uncommon. The oldest conformal surface-exposed ice in northern Greenland is likely located adjacent to Warming Land and may be up to ~55 thousand years old. Basal ice is commonly exposed hundreds of meters from the ice margin and may indicate a widespread frozen basal thermal state. We conclude that the ice margin across northern Greenland offers multiple opportunities to recover paleoclimatically distinct ice relative to previously studied regions in southwestern Greenland.

1. Introduction

Bare ice is exposed subaerially along the margin of the Greenland Ice Sheet (GrIS) for a period of weeks to months each boreal summer, after the previous year's snowfall has melted entirely (Fahnestock and others, 1993). This region – the ablation zone – presently includes more than 12% of the ice sheet by surface area (McGrath and others, 2013). The ablation zone is predicted to expand given continued anthropogenic climate warming, and indeed such an expansion was recently reported and is particularly acute for northern Greenland (Noël and others, 2019). Given downward advection of ice in the accumulation zone and upward advection in the ablation zone, the oldest subaerially exposed surface of an ice mass is generally found along the ice margin, in the ablation zone of land-terminating ice (Hooke, 2005).

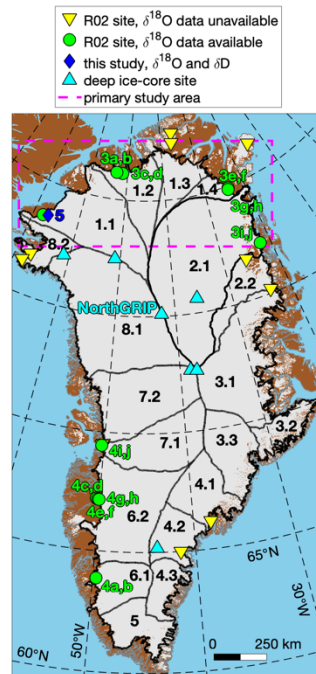
Subaerial exposure of ice from the late Pleistocene epoch was first documented in the ablation zone of the Barnes Ice Cap on Baffin Island by Hooke (1976). There, Pleistocene ice was distinctly whiter than more recent, bluer Holocene ice. Consistent with ice-core records, the stable oxygen-isotope fractionation ratio ($\delta^{18}\text{O}$) of candidate Pleistocene ice was also depleted significantly relative to Holocene

48 ice. For Greenland, between 1985 and 1994 (all years Common Era), Niels Reeh and several collaborators
49 sampled surface ice within the GrIS ablation zone and measured its $\delta^{18}\text{O}$ value. Their goal was to identify
50 sites with inexpensive access to paleoclimatically distinct ice from the late Pleistocene and Holocene
51 epochs (Reeh and others, 2002 and references therein; hereafter R02; Fig. 1). That work resulted in a
52 breakthrough for bulk sampling of paleo-atmospheres, which has since been exploited regularly in
53 Greenland and elsewhere (e.g., Petrenko and others, 2006; Aciego and others, 2007; Schaefer and others,
54 2009; Kurbatov and others, 2010), and it also informed correlation of surface-intersecting internal
55 radiostratigraphy with surface-exposed visible stratigraphy (Kjær and others, 2018).

56 As a result of their sampling campaign, R02 identified a visually distinctive surface stratigraphy
57 along the GrIS margin that enables a broad age classification of exposed ice from the late Pleistocene
58 (~129–11.7 ka, where “ka” means thousands of years ago) and Holocene (11.7–0 ka) epochs. Within the
59 late Pleistocene, this classification includes recent major climate transitions within the Last Glacial Period
60 (LGP; ~115–11.7 ka): the Younger Dryas (YD, 12.8–11.7 ka) stadial, Bølling-Allerød (B-A, 14.7–12.8 ka)
61 interstadial and pre-B-A portion of the LGP (115–14.7 ka) (Rasmussen and others, 2006). This surface
62 stratigraphy is due to spatiotemporal variability in several factors, including the dust concentration in
63 subaerially deposited snow at the time of burial, and the rates of downward vertical advection (burial) in the
64 upstream dry snow zone, horizontal ice flow and upward advection (emergence) in the ablation zone (e.g.,
65 Bøggild and others 1996, 2010; Wientjes and others, 2012).

66
67

Fig. 1



68
69 **Fig. 1.** Map of Greenland identifying all $\delta^{18}\text{O}$ surface-sampling sites reported by R02, including the subset
70 for which $\delta^{18}\text{O}$ data are available and the new Hiawatha Glacier site reported by this study. Green site labels
71 denote figure numbers/panels where each site is further examined. Black numbers denote primary ice-
72 sheet drainage systems (Zwally and others, 2012).

73

74 In recent years, multiple new satellite-borne multispectral sensors have been launched that can
75 reliably detect ablation-zone surface stratigraphy during the melt season with meter to decameter
76 resolution. Here we use Sentinel-2A/B (S2) and WorldView-2/3 (WV) satellite imagery to map the large-
77 scale chronostratigraphy of the northern GrIS margin. We contextualize existing and new *in situ* $\delta^{18}\text{O}$

78 measurements to evaluate correlations between surface ice brightness/color and isotopic composition (and
79 hence apparent ice age). We identify key stratigraphic features of interest, including the apparent location
80 of what is likely the oldest coherent surface-exposed ice in northern Greenland, the geographic pattern of
81 basal ice exposures in northern Greenland and its potential implications for the basal thermal state there.
82

83 **2. Data and methods**

84 **2.1. Satellite imagery and derived products**

85
86
87 Sentinel-2A was launched by the European Space Agency (ESA) in 2015 as a continuation of
88 decades-long international efforts to map global land change, and its twin Sentinel-2B followed in 2017.
89 Their multispectral visible-wavelength sensors have a fine radiometric resolution (12-bit), similar to Landsat-
90 8, enabling reliable detection of subtle changes in surface reflectance at 10-m spatial resolution on a regular
91 basis (e.g., Fahnestock and others, 2016; Yang and others, 2019). While multiple other high-sensitivity
92 visible-wavelength multispectral sensors now exist, including Landsat-8 and the WV constellation, we opted
93 to primarily use S2 imagery for examination of GrIS surface stratigraphy. This selection was made because
94 of its combination of moderate spatial resolution, which simplifies the production of an ice-sheet-wide
95 mosaic, wide across-track swath, frequent revisits during the melt season (effectively ~5-day repeat with
96 both satellites operational), and data availability within our selected processing platform (Google Earth
97 Engine; Gorelick and others, 2017).

98 Since the beginning of S2 operations in mid-2015, the GrIS experienced its most widespread
99 surface melting during the summer of 2019, due to a large high-pressure atmospheric anomaly (Tedesco
100 and Fettweis, 2020). While the major surface chronostratigraphic boundaries are typically within 5 km of
101 the ice margin and are visible at the end of most summer melt seasons, the extensive 2019 melt season
102 provided an opportunity to image a larger expanse of bare ice for an extended period. We leverage this
103 extended exposure of surface ice in the north by constructing a full-resolution mosaic of Greenland based
104 on S2 imagery from August 2019 only.

105 Within Google Earth Engine, we identify all S2 scenes collected over Greenland in August of 2019
106 with a reported cloud-cover fraction of $\leq 15\%$. We use Level-1C S2 scenes (orthorectified, top-of-
107 atmosphere reflectance), which have a pixel-scale geolocation uncertainty that is acceptable for the
108 substantially larger scales of interest in our study. We then define a 10-m grid across Greenland and overlay
109 all available individual scenes, and record the median value of the red, green and blue channels (4, 3 and
110 2, respectively) of those scenes in each grid cell to generate the mosaic. We then apply a gamma correction
111 with a value of 1.5 to enhance low-end contrast. No additional filtering is performed. While the data volumes
112 we analyze remotely are large, our processing chain is simple, with the goal of generating a mosaic of direct
113 value for detecting and mapping surface stratigraphy along the ice margin.

114 For portions of the ice-sheet margin where R02 sampled between 1985 and 1994 (Fig. 1), or where
115 the surface stratigraphy in S2 imagery appears either particularly complex or anomalous, we also examine
116 with WV 1.24- to 2.4-m nadir-resolution 11-bit multispectral imagery. As for S2 imagery, we examine the
117 red, green and blue channels only (5, 3 and 2, respectively) of orthorectified WV images that also have a
118 pixel-scale geolocation uncertainty. This imagery is either from July or August in the most recent available
119 year (2013–2018) and is not contemporaneous with the 2019 S2 mosaic. Although this time difference (up
120 to six years) is a potential source of ambiguity for interpretation, this effect is expected to be minor given
121 slow to negligible ice flow within 5 km of the mostly stable portion of the GrIS margin that is land-terminating.

122 We use two additional higher-level satellite-derived products to facilitate our analysis. For
123 referencing traced layer extents to the ice margin, we vectorize the 15-m-resolution Greenland Ice Mapping
124 Project (GIMP v1) ice mask (Howat and others, 2014; Howat, 2017), which was generated using Landsat-
125 7 ETM+ imagery from 1999 through 2002. This time difference between the GIMP v1 ice margin and our

126 2019 S2 mosaic (up to two decades) is large enough that potential margin migration warrants consideration,
127 especially given independent knowledge of changes in GrIS configuration during this period (e.g., Kjeldsen
128 and others, 2015). Excepting the southwestern sector of Humboldt Glacier, nearly all the margin
129 stratigraphy we traced was across land-terminating ice. We occasionally observed margin migration
130 – nearly invariably retreat – on the order of several S2 pixels (tens of meters), and this pattern seemed to
131 be most common in the vicinity of small proglacial lakes. However, we did not retrace the ice margin of the
132 northern GrIS, as we considered that task beyond the scope of this study. Therefore, we accept this
133 discrepancy may induce a small, spatially variable overestimation of the margin-perpendicular horizontal
134 layer extents discussed below. For high-resolution surface elevations at sites of interest, we use the 10-m-
135 resolution version of the ArcticDEM v7 mosaic, which has an effective time stamp similar to the WV imagery
136 we used (Porter and others, 2018). We assume that ongoing rapid thinning of the northern margin of the
137 GrIS does not significantly affect our use of ArcticDEM as a visual aid for this study (Smith and others,
138 2020a).

139

140 **2.2. Stable isotope transects from surface ice**

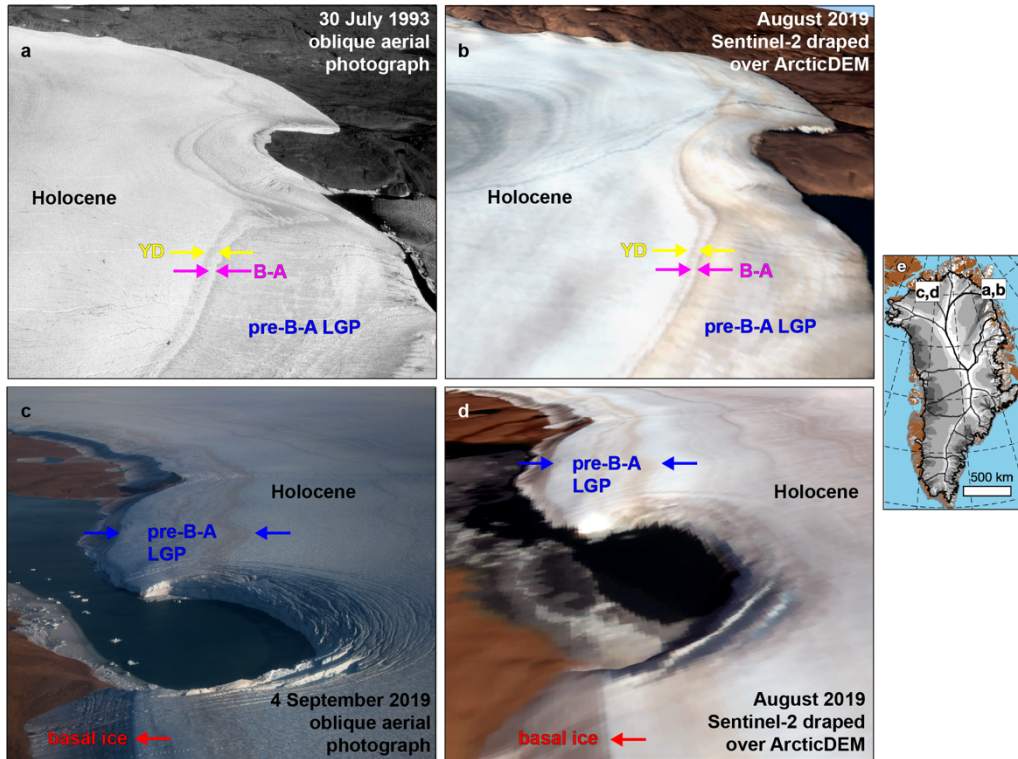
141

142 We base our interpretation of the surface chronostratigraphy of the ice-sheet margin on the
143 correlation identified by R02 between surface optical brightness and $\delta^{18}\text{O}$ measurements of surface-
144 exposed ice (where $\delta^{18}\text{O}$ is a measure of the isotopic fractionation of ^{18}O to ^{16}O , as compared to reference
145 seawater). They hypothesized that patterns in surface brightness relate directly to the ice's age for multiple
146 major climatic periods known to be preserved within the present-day GrIS. R02 supported this hypothesis
147 with a single monochrome photograph depicting the ice-sheet margin in Kronprins Christian Land in
148 northeastern Greenland (their Fig. 2; our Fig. 2a). R02 stated that "*Alternating light- and dark-coloured
149 bands running parallel to the ice margin are visible. The wide dark band nearest to the ice edge is
150 approximately 1 km wide and consists of pre-Holocene ice. The thin light and dark bands adjacent to the
151 wide dark band are the Bølling-Allerød/Younger Dryas climate oscillation. The light-coloured ice to the left
152 is Holocene ice.*"

153

154

Fig. 2



155

156

157

158

159

160

161

162

163

164

165

166

167

168

169

170

171

172

173

174

175

176

177

178

179

180

181

Fig. 2. (a) Oblique aerial photograph of GrIS margin taken 30 July 1993 from near the Kronprins Christian Land K site (Table 1) looking north–northeast (same as Fig. 2 of R02), with R02’s original interpretation superimposed. Credit: H. Oerter. Reprinted from *Annals of Glaciology* with permission from the International Glaciology Society. (b) August 2019 S2 mosaic draped over 10-m ArcticDEM, with perspective and camera position oriented to approximately reproduce panel a and S2 colors contrast-stretched. No vertical exaggeration. (c) Oblique aerial photograph of GrIS margin adjacent to Daugaard-Jensen Land taken 4 September 2019 looking east–northeast, with age interpretation superimposed. Note that the YD and B-A layers are only faintly visible there and were not traced in the S2 mosaic. Credit: J. Sonntag. (d) Same as panel b, but for the site shown in panel c. (e) Map of Greenland showing location of both sites, where grayscale is surface speed as in Fig. 7. Contains Copernicus Sentinel-2 2019 data, processed by ESA.

R02 did not directly georeference $\delta^{18}\text{O}$ values to that oblique aerial photograph, so it was not immediately clear how well this relation holds there or elsewhere, but Bøggild and others (2010) reported patterns of surface dust concentration from this site that were consistent with R02’s hypothesis. The success of later studies of ice-sheet surface geochemistry elsewhere across the GrIS further suggests R02’s hypothesized relation is generally valid for coarsely identifying ice of a desired age (e.g., Petrenko and others, 2006). Fig. 2 shows unambiguously that the qualitative chronostratigraphic interpretation of R02 is reproducible using satellite imagery of Kronprins Christian Land and elsewhere in northern Greenland. Kjær and others (2018) also reproduced the R02 photograph synthetically in a similar manner, from which they further argued that this interpretation is also qualitatively consistent with internal radiostratigraphy where it intersects the ice surface.

In general, the exact positions of R02’s surface $\delta^{18}\text{O}$ transects are not well known, likely because their collection predates widespread use of global navigation satellite systems (GNSS). Further, the azimuths of the surface transects were neither reported nor described, so we assume that they were roughly margin-perpendicular and prescribe these values with a precision of 5° (Table 1). R02 recognized this ambiguity, as not all authors were present during each sampling effort, and they described each site

182 qualitatively with varying degrees of detail. Here we use a database that contains both $\delta^{18}\text{O}$ values and
 183 along-transect distances for multiple R02 sites (H. Oerter, pers. comm., 2018). As needed, we translate the
 184 transect-origin locations manually with a precision of 10 m so that the most margin-proximal sample of each
 185 transect is at the ice-sheet margin (Table 1).

186 In one case (Inglefield Land), the given position is nearly 9 km away from the present ice-sheet
 187 margin, an ambiguity noted by R02. We determined an approximate translation for this site to a location
 188 that is roughly consistent with a photograph of a portion of the margin visited by Risbo and Pedersen (1994),
 189 who performed the sampling there. However, its location is too uncertain and the margin stratigraphy of this
 190 region is too complex to justify comparison of this $\delta^{18}\text{O}$ transect with modern satellite imagery. Hence, we
 191 do not further consider this R02 site.

192

193 **Table 1.** Geographic data and applied translations for R02 $\delta^{18}\text{O}$ surface transects. Sites are ordered
 194 following labeling given in Fig. 1, clockwise from the westernmost Warming Land site. Geographic
 195 coordinates are for the translated transect origin (typically near or at the ice margin). Note that values for
 196 Warming Land sites are updated from R02 (N. Henriksen, pers. comm., 2018), and that site names are
 197 those given by R02. Translation azimuth is the direction in which the transect was translated horizontally,
 198 expressed clockwise from true north. The rightmost three columns are all estimated manually for this study.

Fig. 4/5 Panels	Reeh and others (2002) ice-sheet margin site	Latitude (°N)	Longitude (°W)	Transect azimuth (°)	Horizontal translation (m)	Translation azimuth (°)
4a,b	Warming Land 3	81.1721	53.1600	165	40	0
4a,b	Warming Land 4	81.1721	53.1311	145	50	330
4c,d	Warming Land 1	81.1565	51.4195	175	70	20
4c,d	Warming Land 2	81.1565	51.4661	185	100	170
4e,f	Kronprins Christian Land K	79.9084	24.0531	300	1080	110
4g,h	Kronprins Christian Land KS	79.8517	24.1747	290	530	110
4i,j	Storstrømmen N/NS	77.1865	22.0030	265	1360	285
5a,b	Isortuarssup	63.8724	49.6576	115	1300	160
5c,d	Isunguata Sermia front	67.1868	50.3418	80	960	260
5e,f	Isunguata Sermia margin	67.1628	50.1617	0	150	330
5g,h	Næsset Kangerlussuaq	67.1545	50.0335	100	390	290
5i,j	Pâkitsoq 1/2/3	69.4299	50.2608	120	300	130
—	Inglefield Land	78.0573	67.8978	155	8790	165

199

200 In late July 2019, we collected one additional surface transect near the southwest corner of
 201 Hiawatha Glacier, adjacent to Inglefield Land (Fig. 1), to better understand the chronostratigraphy of this
 202 complex margin. Ice samples were collected in a manner similar to that described by R02, i.e., several
 203 centimeters of surface crust were removed with an ice axe, then ice was chipped from the underlying solid
 204 surface and placed into 60-mL polypropylene bottles. We collected 84 samples with a mean separation of
 205 9.5 m and sampling locations were recorded with a Geode™ mapping-grade GNSS receiver with sub-meter
 206 accuracy. The ice was then melted and both $\delta^{18}\text{O}$ and δD (^2H to ^1H isotopic ratio) values of the resulting
 207 meltwater were measured by a mass spectrometer at University of Oulu.

208

209 2.3. Layer tracing

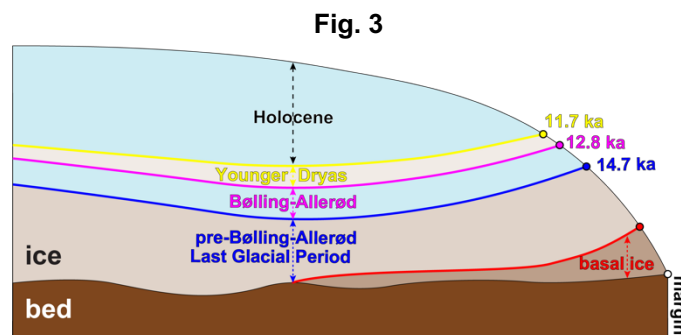
210

211 To map potential chronostratigraphic units (layers) within the S2 mosaic based on contrasts in
212 apparent surface brightness and color, we examined the ice-sheet margin within the mosaic at a 1:10,000
213 scale in QGIS version 3. We used local contrast stretching to improve visual boundary identification
214 (typically min./max. stretch to 2–98% cumulative count), and traced boundaries manually. Where such
215 boundaries were ambiguous, we did not trace them. We briefly explored alternative automated tracing
216 schemes, including spectral band ratios, to identify individual layers. However, such schemes were typically
217 challenged by variable cloudiness, solar elevation angle and the quality of preliminary versions of the
218 mosaic, so we consider further development thereof beyond the scope of the present study. Our manual
219 tracing approach is somewhat analogous to that of MacGregor and others (2015), who traced GrIS
220 radiostratigraphy semi-automatically. We sacrifice deeper investigation of methodological sophistication
221 and automation, which may enable rapid scalability in the future, so that a first, large-scale evaluation of
222 northern GrIS margin surface stratigraphy can be generated.

223 Here we focus primarily on the boundaries that separate the four layers identified visually or
224 described by R02. While additional visually distinctive layers are observed that appear to originate from
225 both within and before the Holocene, these layers are not as widespread across the northern GrIS, nor
226 were they identified visually by R02, nor were candidate ages assigned to them by that study.

227 We next describe these four boundaries in their typical stratigraphic order from top (highest
228 exposed and farthest from the margin) to bottom (lowest exposed, at or closest to the margin). Fig. 3 shows
229 a simple ice-sheet cross-section illustrating these boundaries. The first boundary we traced is the bottom
230 of the Holocene layer (i.e., its lowermost limit, 11.7 ka), which is identified by the characteristic sharp
231 transition between white and light brown ice (Bøggild and others, 2010). The second is the bottom of the
232 YD layer (12.8 ka), which directly underlies the Holocene layer, is typically a light brown color and is
233 relatively thin, i.e., the length of its margin-perpendicular horizontal exposure rarely exceeds ~200 m. This
234 particular boundary is harder to trace because it is often less distinct than the others and it is closely
235 sandwiched between the above Holocene boundary and the next meteoric boundary below it. The third
236 boundary is the bottom of the B-A layer (14.7 ka), which is the bottom of the thin white layer that separates
237 the dustier/browner YD layer above it from the darker brown pre-B-A LGP ice beneath it. Finally, we traced
238 the upper boundary of what we assume is basal ice, which is significantly darker and grayer than the
239 overlying Holocene or pre-Holocene ice and is typically not conformal to those meteoric strata. Hence, it
240 has no specific age, although it typically underlies what appears to be pre-Holocene ice from within the LGP
241 (115–11.7 ka). Tracing this boundary enables both better estimates of the horizontal length of surface-
242 exposed pre-Holocene meteoric ice – rather than only using the ice margin – and also an opportunity to
243 more broadly contextualize these basal ice exposures.

244
245



246 **Fig. 3.** Simplified cross-section of the margin of the northern GrIS illustrating the typical chronostratigraphy
247 we mapped (circles). Boundary colors are the same as used for other figures. Not all boundaries were
248 always detected, nor were they always found in this stratigraphic order due to occasional folding. Ice color
249 is exaggerated and approximates that which we observed following local contrast stretching when mapping
250 boundaries at 1:10,000 scale.
251

252
253
254
255
256
257
258
259
260
261
262
263
264
265
266
267
268
269
270
271
272
273
274
275
276
277
278
279
280
281
282
283
284
285
286
287

For WV imagery adjacent to Hiawatha Glacier and Warming Land, we retraced the four boundaries described above at finer scales (between 1:1,000 and 1:2,500), leveraging the finer resolution permitted by that imagery. For two locations adjacent to Warming Land, we also traced additional boundaries between alternating layers of whiter and browner ice in pre-B-A LGP ice that are not as distinct in the coarser-resolution S2 imagery.

To calculate plan-view distances between traced boundaries (the surface-exposed, horizontal layer thickness; not corrected for slope), we first determine the shortest distance between each digitized point and the ice margin or nunatak perimeter, whichever is closest. For each traced boundary, we then determine where each lower boundary (i.e., more margin-proximal) intersects the line that connects each of the upper boundaries' digitized points and the ice margin. In doing so, we approximate the margin-perpendicular horizontal exposure of each "layer" (stratigraphic unit between traced boundary pairs). All reported distances/thicknesses are great-circle arclengths on the surface of the WGS84 ellipsoid, not cartesian distances within our default projection (EPSG:3413), which can differ by >2% at 80°N for the spatial scales we consider.

2.4 Ice-core data

To evaluate the apparent age of pre-B-A LGP ice, we use the NorthGRIP ice-core dust-concentration record produced by Ruth and others (2003) using a laser microparticle detector. This record covers the time span between 60 and 9.5 ka, which is fortuitously contemporaneous with plausible chronostratigraphic interpretations of satellite imagery along part of the northern GrIS margin. While the interactions between dust, algae and seasonal subaerial melting are an area of active research (e.g., Ryan and others, 2018), for the purposes of this study we assume that the marginal surface stratigraphy whose boundaries we mapped can be compared qualitatively to this ice-core dust record from the dry snow zone (e.g., Bøggild and others, 2010).

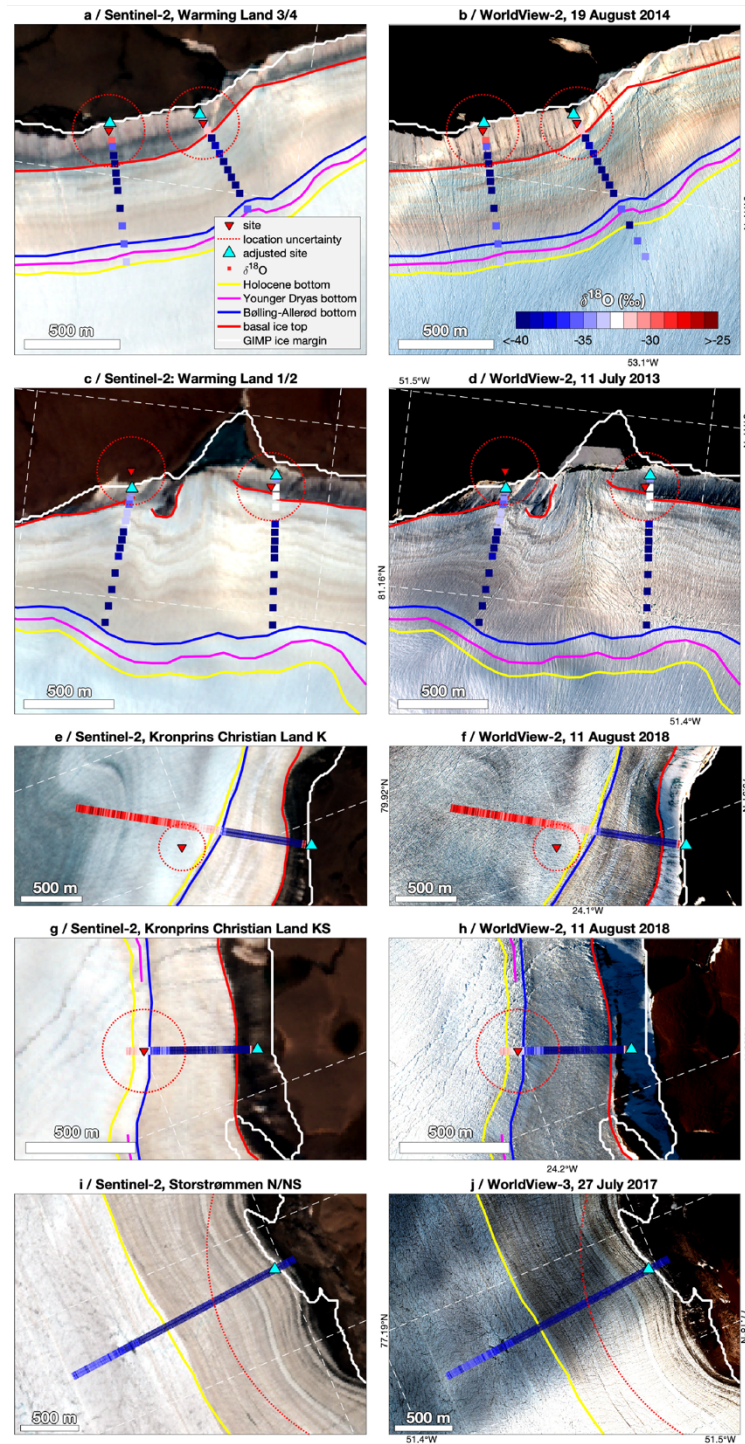
3. Results

3.1. Satellite imagery at $\delta^{18}\text{O}$ transects

Figs. 4, 5 and 6 show both the 2019 S2 mosaic and WV imagery in the vicinity of the available surface $\delta^{18}\text{O}$ transects across the GrIS. These comparisons demonstrate that S2 and WV detect fundamentally the same margin stratigraphy. This consistency indicates that the coarser-resolution S2 imagery is sufficient to map key boundaries in surface stratigraphy across the GrIS.

288

Fig. 4

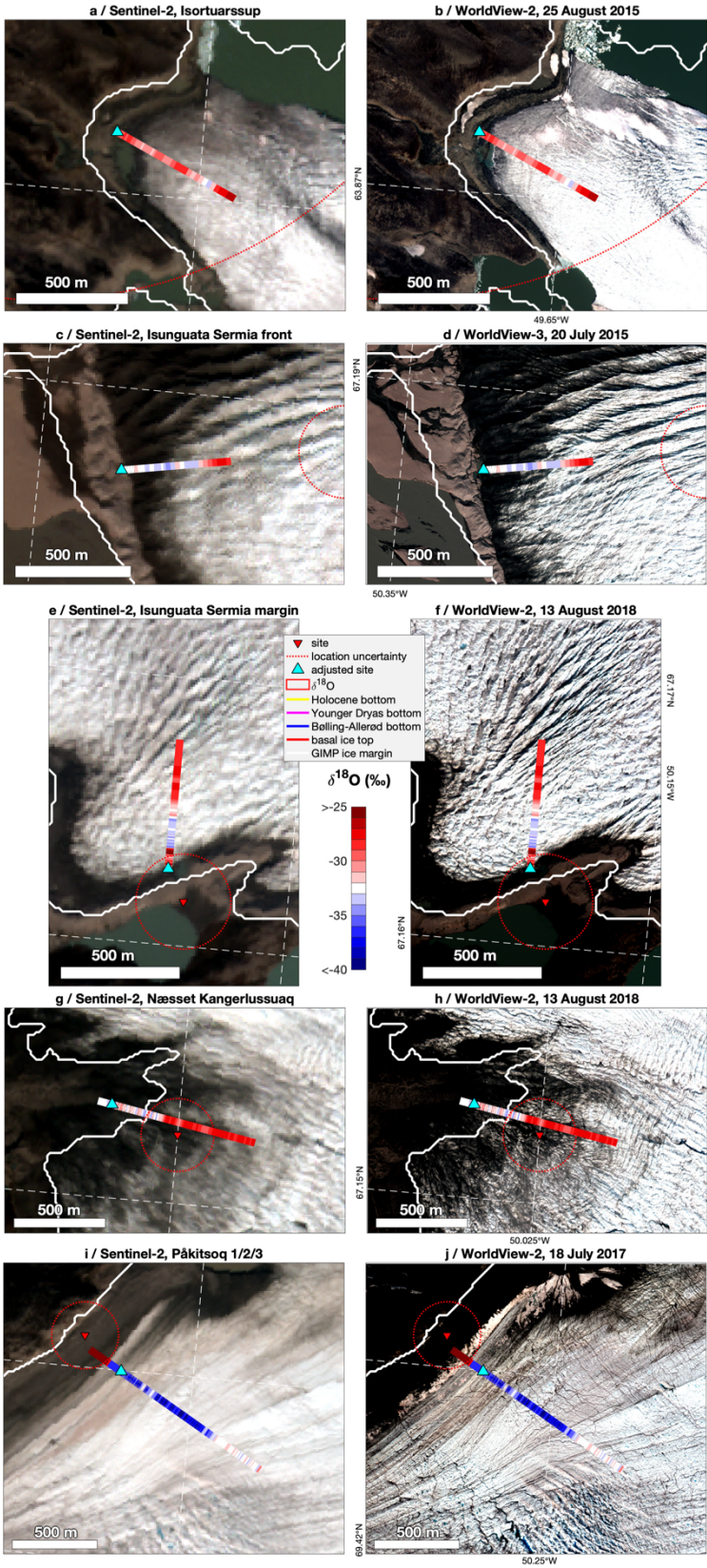


289
 290
 291
 292
 293

Fig. 4. August 2019 S2 mosaic (left of pair) and WV imagery (right of pair) in the vicinity of available R02 $\delta^{18}\text{O}$ surface-sampling sites in northern Greenland (Fig. 1), with $\delta^{18}\text{O}$ data overlain at manually corrected position (“adjusted site”), each transect’s location uncertainty, and boundaries traced in S2 mosaic only shown for each pair. All image subscenes are contrast-stretched. For panels f and h, brighter snow remains

294 along the margin that obscures the darker basal ice (evident in panels e and g), as was also observed in
295 this region by Bøggild and others (2010). WV sensor and image date is given in the title. Contains
296 Copernicus Sentinel-2 2019 data, processed by ESA. WV imagery is copyright 2020 DigitalGlobe Inc.
297

Fig. 5



300 **Fig. 5.** August 2019 S2 mosaic (left of pair) and WV imagery (right of pair) in the vicinity of available R02
301 $\delta^{18}\text{O}$ surface-sampling sites in southern Greenland (Fig. 1). Format follows Fig. 4. Contains Copernicus
302 Sentinel-2 2019 data, processed by ESA. WV imagery is copyright 2020 DigitalGlobe Inc.
303

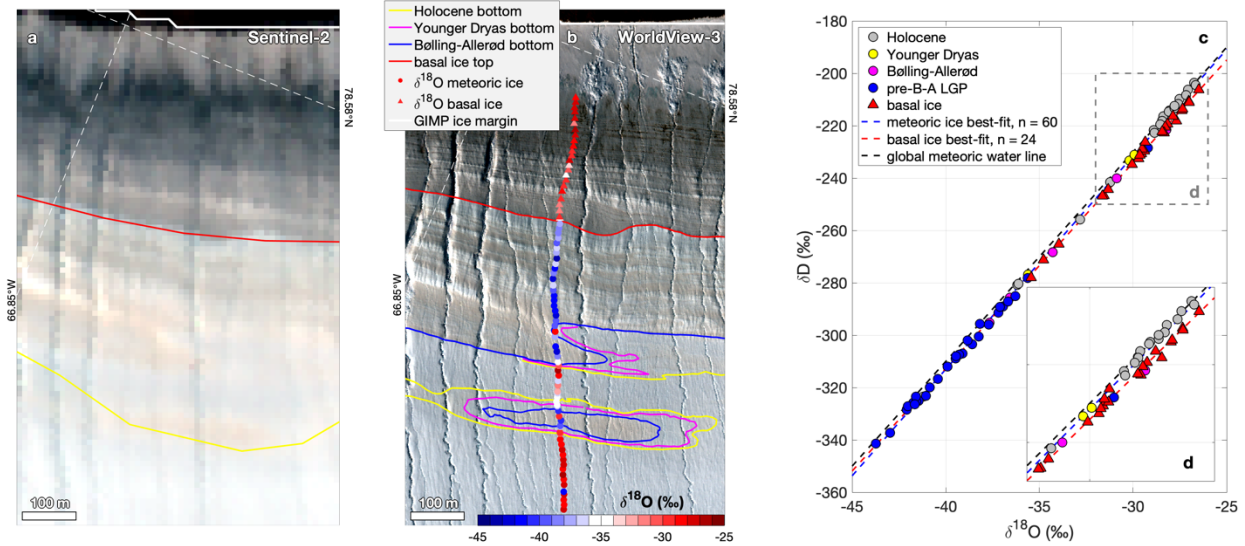
304 From these subscenes, it is clear that distinct margin surface strata are typically both more coherent
305 and resolvable in northern Greenland, regardless of apparent age and potential sampling bias in the site
306 selection of R02. While such strata have been identified reliably in southern Greenland previously from
307 ground-based sampling and low-altitude aerial mapping (Petrenko and others, 2006; Kurbatov and others,
308 2010), their surface expression in southern Greenland is ambiguous in the satellite imagery we examined,
309 even in the finer resolution WV imagery. Only at the Pâkitsoq site, near where Petrenko and others (2006)
310 sampled, is there a hint of coherent but heavily folded pre-Holocene strata in the WV imagery (Fig. 5j).

311 When compared against the estimated locations of the $\delta^{18}\text{O}$ transects, we find that only the
312 Kronprins Christian Land K/KS sites in northeastern Greenland display a plausible relation between $\delta^{18}\text{O}$
313 and surface stratigraphy at the scale of these subscenes (Fig. 4e-h). There, the transects are finely sampled
314 (≤ 5 m), the boundaries between the Holocene, YD and B-A layers are clear, and there is a clear transition
315 in $\delta^{18}\text{O}$ values between the LGP and the Holocene. The imprecision of available georeferencing and
316 translation uncertainty prevent a finer-scale assessment of the relation between $\delta^{18}\text{O}$ and the layering
317 between the beginning of the B-A and the Holocene. At other sites in northern Greenland, either the
318 coarseness of the $\delta^{18}\text{O}$ sampling (Warming Land 1-4, Fig. 4a-d), the length of the transect (Warming Land
319 1-4, Fig. 4a-d), the imprecision of the georeferencing (Inglefield Land) or the lack of a clear transition in
320 $\delta^{18}\text{O}$ values, perhaps related to periodic surging (Storstrømmen N/NS, Fig. 4i,j; Mougnot and others, 2018)
321 prevent additional confirmation of the large-scale chronostratigraphic relation hypothesized by R02. This
322 situation limits us to Kronprins Christian Land K/KS as the type locality for the large-scale $\delta^{18}\text{O}$ –stratigraphy
323 relation that we seek to exploit (Fig. 2), but we note that this restriction does not impact interpretation of the
324 previously mentioned finer-scale investigations in southwestern Greenland (e.g., Pâkitsoq).

325 The new Hiawatha Glacier transect we collected is not as finely sampled as that of the R02
326 Kronprins Christian Land sites and its margin stratigraphy is more complex, with repeated sequences
327 indicating folding (Fig. 6). However, its transitions in $\delta^{18}\text{O}$ and δD values match well with satellite-mapped
328 transitions in visual appearance, strongly supporting the $\delta^{18}\text{O}$ –stratigraphy relation hypothesized by R02.
329 The $\delta^{18}\text{O}$ and δD values are not perfectly bimodal between glacial and interglacial periods, but that is
330 expected given the significant variability that is typically present in those values. Further, the best-fit $\delta^{18}\text{O}$ –
331 δD relation differs significantly between meteoric ice (8.14 ± 0.07 ; 95% confidence bound) and what we
332 assumed was basal ice prior to sampling (7.85 ± 0.18). Although this difference is small compared to global
333 variability in that relation (e.g., Putman and others, 2019), it is consistent with previous observations of the
334 isotopic differences between meteoric and basal ice (Larsen and others, 2010), further indicating that this
335 layer is not meteoric.
336

337

Fig. 6



338

339

340

341

342

343

344

345

346

347

348

Fig. 6. (a) August 2019 S2 mosaic and (b) 24 August 2018 WV image at the southwestern corner of Hiawatha Glacier, with $\delta^{18}\text{O}$ values measured from surface ice samples collected in July 2019 overlain. Image sub-scenes are contrast-stretched. Boundary tracings shown are those mapped using each respective image, i.e., they were traced at substantially different spatial scales. (c) $\delta^{18}\text{O}$ - δD co-isotope plot with values subdivided by margin region where they were detected. Reference global meteoric water line is from Craig (1961). (d) Zoom-in of isotopic difference between meteoric and basal ice samples. Contains Copernicus Sentinel-2 2019 data, processed by ESA. WV imagery is copyright 2020 DigitalGlobe Inc.

3.2. Margin layer mapping

349

350

351

352

353

354

355

356

357

358

359

360

361

362

Our S2 mapping of the bottom of the Holocene, YD and B-A layers, along with the top of the basal ice, generated 242, 144, 145 and 241 discontinuous segments, respectively. These boundaries were mapped as far north as 82.1°N, adjacent to Peary Land in northern Greenland, and as far south as 74.2°N, adjacent to Waltershausen Glacier in eastern Greenland, but the boundary was mostly mapped north of 76.8°N. In terms of well-known major outlet glaciers in northern Greenland, we mostly mapped these boundaries from west of Hiawatha Glacier (northwest) to Storstrømmen (northeast). In terms of ice-drainage systems (Fig. 1), nearly all of the layer segments we mapped were within ice-drainage systems 1.1, 1.2, 1.3, 1.4 and 2.1, with a small portion mapped within system 2.2 (Zwally and others, 2012).

363

364

365

366

367

368

369

370

For the bottom of the Holocene layer, the median and maximum segment lengths are 4.2 and 89.5 km, respectively, with a median separation between digitized points of 91 m. The YD, B-A and basal ice boundaries were less extensively observed and mapped. Their median separation between digitized points was similar (79, 99 and 108 m, respectively), but their median segment lengths were somewhat shorter (1.7, 3.6 and 2.8 km, respectively) and their maximum segment lengths were substantially shorter (26.6, 44.3 and 39.4 km, respectively).

371

372

373

374

375

376

377

378

379

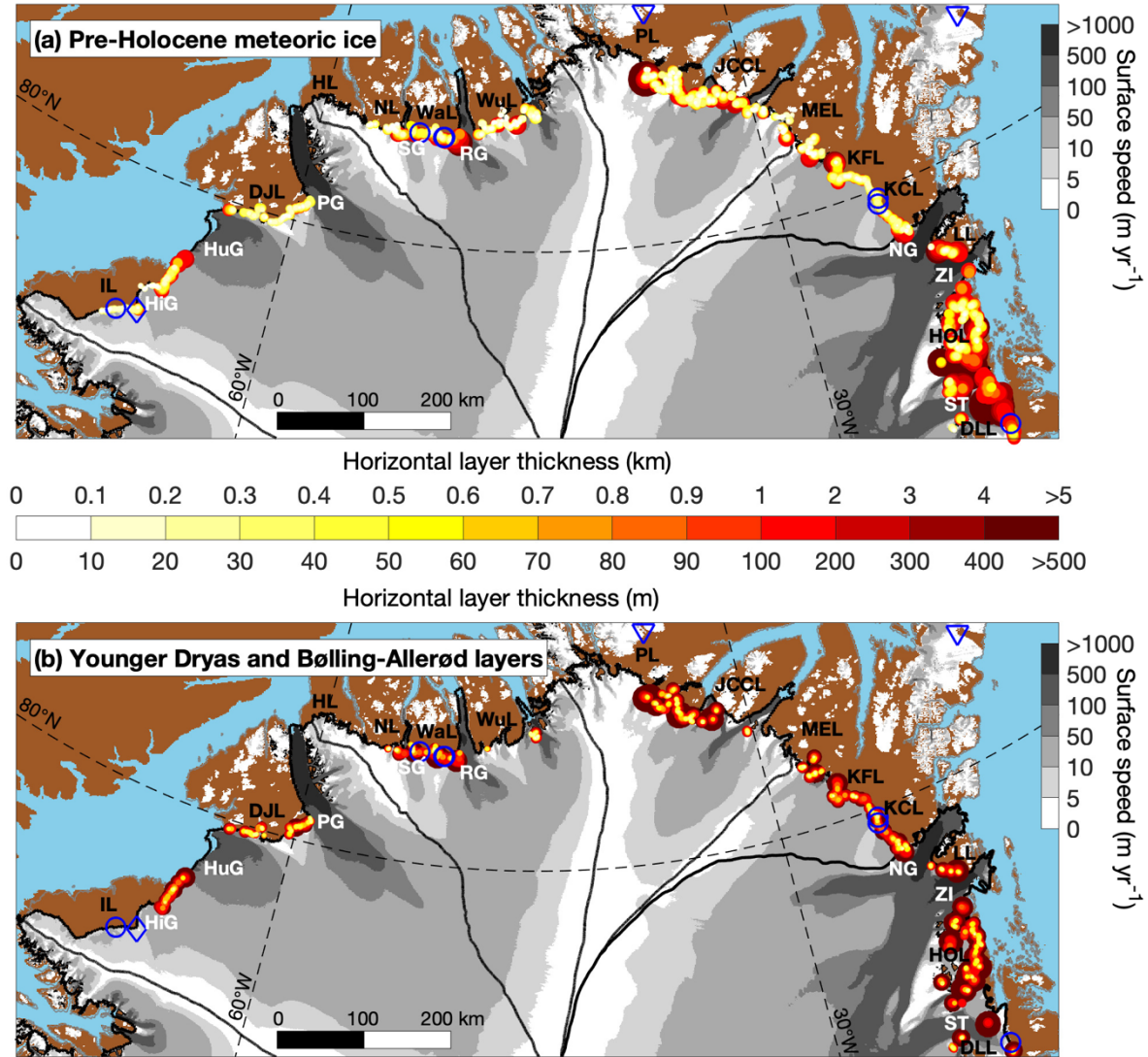
380

Fig. 7 shows two combinations of the horizontal layer thickness between mapped boundaries. In the case of the pre-Holocene meteoric ice thickness, this metric represents an indirect proxy for the potential maximum age of coherent surface stratigraphy originating from periods of general interest. We note that this proxy is complicated by multiple factors, including the surface slope, subsurface boundary dip and the presence of any anomalous margin structures (e.g., plan-view folds). The combined thickness of the YD and B-A layers constitute a fixed period (1.1 + 1.9 = 3.0 kyr) that represents an indirect proxy for the age resolution within that period. While the resolution of the Landsat imagery used to generate the GIMP ice mask is 15 m and that of the S2 imagery is 10 m, we consider these thicknesses to have an uncertainty

371 smaller than or comparable to that of the along-boundary digitization separation (~100 m). This uncertainty
 372 is due to both the precision of our tracing and uncertainty in delineation of the ice margin, which was traced
 373 in imagery nearly two decades older than that which we investigated (§2.1).

374
 375

Fig. 7

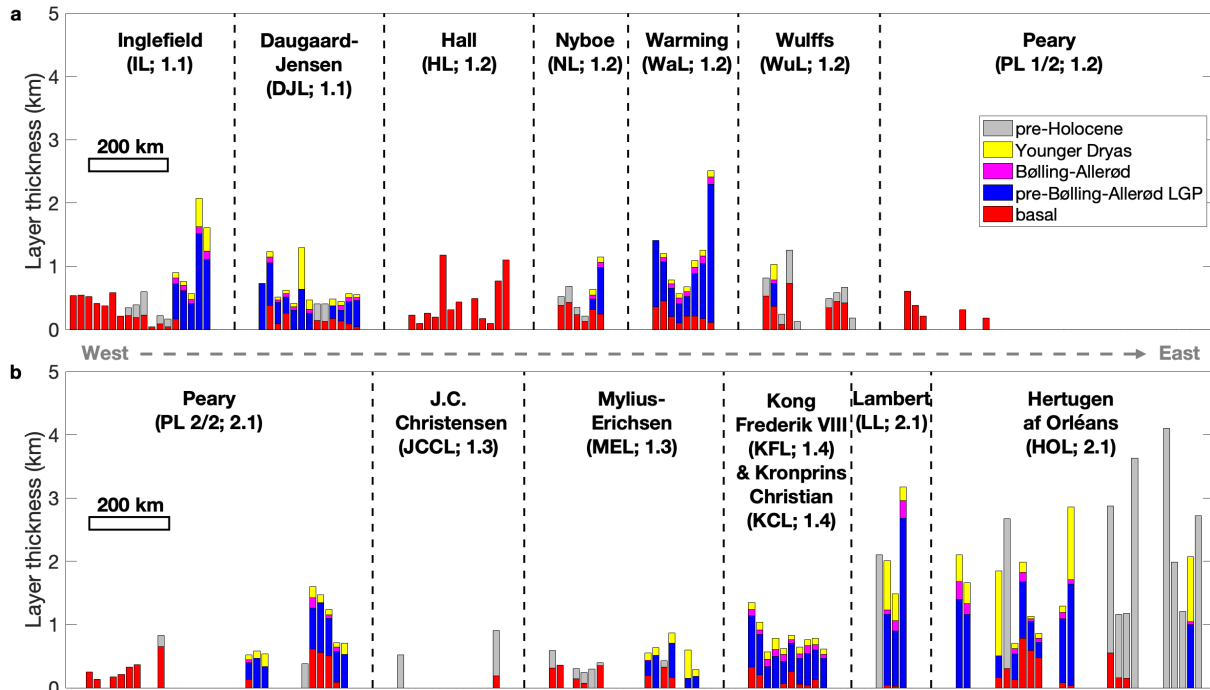


376
 377 **Fig. 7.** (a) Horizontal thickness (distance) between the traced bottom of the Holocene layer and either the
 378 ice margin, nearby nunataks or the traced top of the basal ice layer, whichever is closest. Background gray
 379 scale on ice is surface speed (Joughin and others, 2017), and thick black lines are ice-drainage systems
 380 (Zwally and others, 2012). Layer-thickness symbols are scaled by both size and color, with smaller values
 381 shown above larger ones. (b) Same as panel a but the horizontal thickness between the traced bottoms of
 382 the Holocene and B-A layers, i.e., the combined horizontal thickness of the YD and B-A layers. Note values
 383 assigned to thicknesses differ between panels a and b, per values on top and bottom of color scale,
 384 respectively. Blue symbols denote R02 sites following Fig. 1. Abbreviations in panel a for regions/glaciers:
 385 IL: Inglefield Land; HiG: Hiawatha Glacier; HuG: Humboldt Glacier; DJL: Daugaard-Jensen Land; PG:
 386 Petermann Glacier; HL: Hall Land; NL: Nyboe Land; SG: Steensby Glacier; WaL: Warming Land; RG:
 387 Ryder Glacier; WuL: Wulffs Land; PL: Peary Land; JCCL: J.C. Christensen Land; MEL; Mylius-Erichsen

388 Land; KFL: Kong Frederik VIII Land; KPL: Kronprins Christian Land; NG: Nioghalvfjerdingsfjorden Glacier;
 389 LL: Lambert Land; ZI: Zachariæ Isstrøm; HOL: Hertugen af Orléans Land; ST: Storstrømmen; DLL:
 390 Dronning Louise Land.

391
 392 The median horizontal thickness of pre-Holocene meteoric ice that we mapped is ~714 m (Fig. 7a,
 393 Fig. 8). This thickness is typically smaller in northwestern Greenland, as compared to northeastern
 394 Greenland. At lower latitudes in northeastern Greenland (<78°N), this thickness sometimes exceeds 2 km.
 395 However, these estimates are biased by more complex margin stratigraphy (folding) and the greater
 396 presence of nunataks there (e.g., Fig. 12, Appendix A; §3.3). Not all nunataks we observe in the S2 mosaic
 397 are present in the GIMP ice mask, leading to occasional spuriously high values we could not filter out easily.
 398 The thickest (in the margin-perpendicular sense) exposures of pre-Holocene ice occur along the GrIS
 399 margin adjacent to northeastern Inglefield Land, southern Daugaard-Jensen Land, southern Warming
 400 Land, southeastern Peary Land, southwestern Mylius-Erichsen Land, western Kong Frederik VIII Land,
 401 southwestern Kronprins Christian Land and the nunataks of Hertugen af Orléans Land south of Zachariæ
 402 Isstrøm (Fig. 7a, Fig. 8). Elsewhere, such as southwestern Inglefield Land, such exposures can be near-
 403 contiguous for tens of kilometers, but their margin-perpendicular length is shorter and harder to interpret.
 404

405 **Fig. 8**



406 **Fig. 8.** Binned median horizontal thickness of each mapped layer (distance between either two traced
 407 boundaries or one traced boundary and ice margin), separated regionally by margin-adjacent land (vertical
 408 dashed lines) Abbreviations follow Fig. 7, and the number afterward is the GrIS drainage basin following
 409 Fig. 1. Along-margin bin length is 20 km. The horizontal scale bar panel is valid only within each land, i.e.,
 410 it is not continuous between lands and there is an artificial 100-km buffer between each land’s mapped
 411 exposures. Where the bottom (beginning) of the Holocene was mapped, but no other conformal boundaries
 412 below (older) than that, the layer is classified as “pre-Holocene”. (a) Western half of our study area, including
 413 the western half of Peary Land (“PL (1/2)”). (b) Eastern half of our study area, beginning with the eastern
 414 half of Peary Land (“PL (2/2)”). Note that these thickness distributions filter out nunatak-adjacent traced
 415 boundaries as best as possible, so Dronning Louise Land is not shown.
 416

417

418 The median horizontal thicknesses of the YD and B-A layers were not significantly different (81 and
419 85 m, respectively), and their total median thickness (161 m; Fig. 7b) was less variable across the northern
420 GrIS than the total thickness of pre-Holocene meteoric ice. We attribute this difference in spatial variability
421 to two factors: 1. Their combined median thickness is only ~16 S2 pixels, so it was sometimes difficult to
422 resolve at the fixed map scale we selected for mapping, and thinner exposures of these layers are likely
423 undersampled. 2. This layer pair represents a fixed period of time (3 kyr), whereas the total thickness of
424 pre-Holocene meteoric ice has no fixed period and may vary by tens of thousands of years. At the 10-m
425 resolution of S2, the westernmost extent of detectable, coherent YD and B-A layers is northeastern
426 Inglefield Land (Fig. 8), along the northeastern corner of Hiawatha Glacier; the easternmost extent is near
427 Storstrømmen in Dronning Louise Land.

428

429 **3.3. Anomalous margin layering**

430

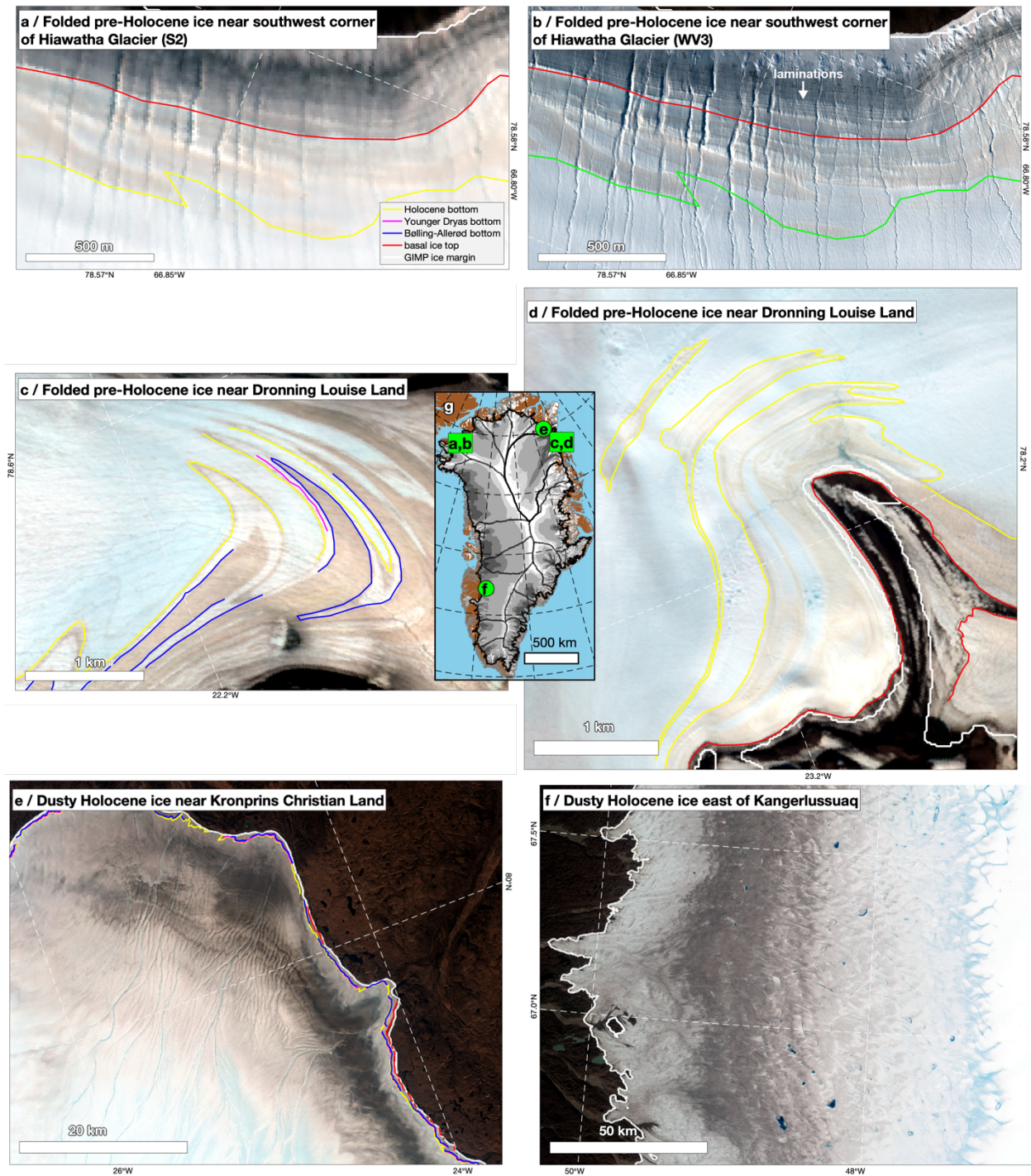
431 Having mapped the large-scale margin chronostratigraphy of the northern GrIS, we next briefly
432 document anomalous and notable expressions of that stratigraphy (Fig. 9), in particular folded or unusually
433 dark ice.

434 With one major exception, the map trace of the pre-Holocene stratigraphy in the northwestern half
435 of our study area (i.e., west of 45°W) generally conforms to either the ice margin or the mapped exposure
436 of basal ice (Fig. 12). This exception is the ~35-km stretch of the ice margin immediately west of the
437 southwestern corner of Hiawatha Glacier, Inglefield Land. There, the bottom of the Holocene undulates
438 along-margin at kilometer scales with no discernible relation to the relatively uniform exposure of basal ice.
439 Examination of both the S2 mosaic and finer-resolution WV imagery confirms this pattern and that the
440 bottom of the Holocene ice appears to be repeated perpendicular to the ice margin at a scale of ~200 m
441 (Figs. 6 and 9a,b). In map view, a portion of the pre-Holocene LGP sequence – but not all of it – is
442 interfingered with Holocene ice. This pattern indicates that the Holocene–LGP boundary is steeply folded
443 there relative to the surface slope, consistent with both the radar-sounding observations of Kjær and others
444 (2018) and the cross-sectional view put forth by Schaefer and others (2009) for a similar pattern within a
445 smaller exposure in southwestern Greenland. The origin of this disturbance is unknown, but any plausible
446 explanation must account for the remarkable horizontal extent of the folding and its apparent synchronicity.

447

448

Fig. 9



449

450

451

452

453

454

455

456

Fig. 9. Subscenes of contrast-stretched August 2019 S2 mosaic (except panel b, which is WV) showing example anomalous margin structures and layering across Greenland. (a) The ice-sheet margin southwest of Hiawatha Glacier in northwestern Greenland showing regular folding of pre-Holocene ice. (b) Same as panel a but using WV imagery. (c) and (d) Apparent plunging folds in emerging stratigraphy at the ice-sheet margin near Dronning Louise Land in northeastern Greenland. (e) The ice sheet bordering Kronprins Christian Land in northeastern Greenland and (f) east of Kangerlussuaq in southwestern Greenland showing similar gray high-dustiness regions within Holocene ice. (g) Map of Greenland showing location of

457 subscenes, where grayscale is surface speed as in Fig. 7. Contains Copernicus Sentinel-2 2019 data,
458 processed by ESA. WV imagery is copyright 2020 DigitalGlobe Inc.

459

460 East of $\sim 32^{\circ}\text{W}$, plan-view lateral folding of identifiable boundaries occurs intermittently and mostly
461 along the margins of outlet glaciers and nunataks (e.g., Fig. 9c,d). This pattern suggests a plunging fold in
462 the layering, i.e., one whose fold axis has a non-negligible dip relative to the near-horizontal ice surface.
463 These folds could arise from past variability in the local ice-flow velocity field, as has been inferred for
464 medial moraines at larger scales on Malaspina Glacier, Alaska (Post, 1972; Hudleston, 2015). However,
465 given that these folds are often seen near nunataks, which indicate locally non-negligible subglacial
466 roughness, we consider it more likely that they are due to significant lateral shear as ice flows around these
467 obstacles.

468 In part of northeastern Greenland, north of Nioghalvfjærdsfjorden Glacier, we observe the extent of
469 an unusually dark exposure of ice that clearly originated during the Holocene epoch and was previously
470 identified by Bøggild and others (1996) (Fig. 9e). This dark ice is typically found within a layer that lies
471 between $\sim 2\text{--}5$ km inland of the traced bottom of the Holocene and is adjacent to Kronprins Christian Land,
472 where the type locality for the chronostratigraphic relation was first identified by R02 (Fig. 2). While we
473 cannot yet assign a specific age range to this layer, its expression qualitatively resembles that of the better-
474 known dark layer in southwestern Greenland (Fig. 9f), which also appears to be partly related to Holocene
475 dust present in the ice (Bøggild and others, 1996; Wientjes and others, 2012; Ryan and others, 2018).

476

477 **3.4. Potential oldest surface-exposed ice in Greenland**

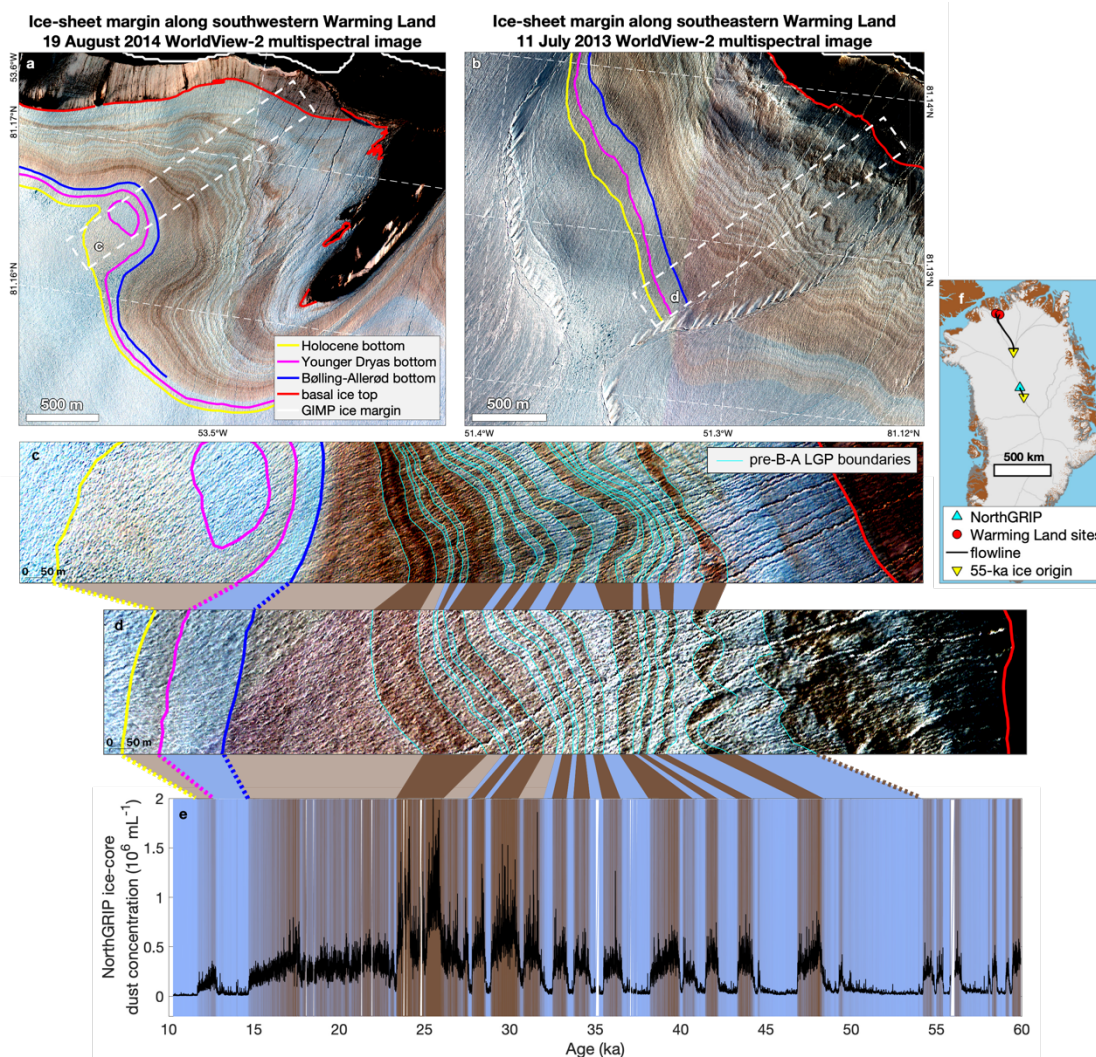
478

479 A question that naturally arises from our mapping is: where is the oldest ice? Our coarse mapping
480 of chronostratigraphy of the northern GrIS margin reveals two distinct sites with extensive and coherent
481 pre-Holocene stratigraphy that are ~ 38 km apart and adjacent to Warming Land (Fig. 10; Figs. 13 and 14,
482 Appendix A). Warming Land is the mostly deglaciated region bounded by Steensby Glacier to the west and
483 Ryder Glacier to the east, both of which are major marine-terminating outlet glaciers in northern Greenland
484 (Fig. 7a). At both sites, more than 20 $>10\text{-m}$ -wide layers below the B-A are distinguishable and mostly
485 conformable with each other. We distinguish these layers by their alternating pattern of color and
486 brightness, and they are typically detectable for several kilometers along-margin. For pre-B-A LGP layers
487 at these two sites, there is no indication of plan-view folding, as observed elsewhere in northern Greenland
488 (e.g., Fig. 9c,d). This pattern suggests that layering at these sites is not repeated due to folding, but instead
489 represents a contiguous period of ice deposition and subsequent flow.

490

491

Fig. 10



492 **Fig. 10.** Contrast-stretched WV multispectral imagery of the GrIS margin adjacent to (a,c) southwestern
 493 and (b,d) southeastern Warming Land, in northern Greenland between Steensby and Ryder glaciers. Boxes
 494 between panels c and d identify potential matches in periods of higher apparent dust concentration between
 495 the two sites and (e) the dust concentration measured in the NorthGRIP ice core (Ruth and others, 2003).
 496 In panel e, background color is scaled between blue (low dust concentration) and brown (high dust
 497 concentration) to illustrate potential matches. (f) Map of Greenland showing location of relevant sites and
 498 estimated upstream origin of 55-ka ice, calculated using a Greenland-wide surface-velocity field (Joughin
 499 and others, 2017) and a shape factor of 0.8. WV imagery is copyright 2020 DigitalGlobe Inc.
 500
 501

502 Because we hypothesize that the layers' color and brightness is primarily due to variable englacial
 503 dust concentration, following Bøggild and others (2010), we compared the Warming Land sites' layering to
 504 the nearest available multi-millennial ice-core record of dust concentration, which is from the NorthGRIP
 505 ice core located more than 700 km southeast of these two sites (Fig. 10e,f). We briefly explored the
 506 mathematical relation between NorthGRIP dust concentration and WV-observed color but could not
 507 establish a simple relation, so this possibility is left to future investigations. Nevertheless, a qualitative but
 508 surprisingly good visual relation is apparent between the two sites' layering and the NorthGRIP dust record.
 509 Alternating browner and bluer layers exposed near Warming Land appear to be sequenced consistently

510 with dustier and cleaner periods, respectively, in the NorthGRIP ice core. Further, the longer the dusty
511 period in the NorthGRIP record, the wider the exposed dusty layer at Warming Land, with the same relation
512 holding generally for less dusty periods and cleaner layers. We therefore hypothesize that the age of LGP
513 ice exposed at these two sites extends back in time to a period well before the Bølling-Allerød interval
514 (i.e., older than 14.7 ka) – perhaps to before ~55 ka – and that multiple Dansgaard–Oeschger events are
515 recorded there. While this apparent relation sets aside potential complexity inherent to tens of millennia of
516 ice flow between deposition in the ice-sheet interior and present-day emergence at the margin, this
517 hypothesis can simply explain the remarkable correspondence between these independent records.

518 While R02 hypothesized the presence of surface-exposed ice from the Last Interglacial Period
519 (Eemian; ~130–115 ka) elsewhere on the GrIS margin, that inference could not be confirmed by $\delta^{18}\text{O}$
520 measurements alone. Hence, we suggest that the Warming Land sites discussed above represent the
521 oldest coherent exposures of late-Pleistocene ice in the northern hemisphere identified so far. In Antarctica,
522 yet older surface-exposed ice has been found in blue ice regions and the Dry Valleys (e.g., Schäfer and
523 others, 2000; Sinisalo and Moore, 2010; Buizert and others, 2014; Yan and others, 2019).

524

525 **3.5. Basal ice properties**

526

527 During our satellite mapping of margin layering, we made four main observations of the basal ice
528 layer that warrant reporting here. While we examined the northern GrIS margin at fine spatial scales, we
529 also conducted a larger-scale examination of the whole of the GrIS margin. We found that the basal ice
530 exposures detectable in the S2 mosaic were much more common in northern Greenland (our study area)
531 than elsewhere. So, while we do not consider our mapping of the top of the basal ice to be comprehensive
532 for the whole of Greenland, we consider it sufficient to support the following observations.

533 The first observation is that – when examined in finer-resolution WV imagery – the basal ice layer
534 is itself laminated at multi-meter scales, as also reported by R02 but now visible at larger scales (e.g., Fig.
535 9b). This pattern is typically margin-parallel and suggests that the basal ice layer was formed episodically.
536 It is not immediately clear if this pattern is consistent with the laminated basal ice facies that are sometimes
537 observed *in situ* (e.g., Knight, 1997). During our sampling at Hiawatha Glacier (Fig. 6), we also observed
538 sub-meter laminations in the basal ice. Where supraglacial streams incised into the basal ice, these
539 laminations were steeply dipping (subvertical).

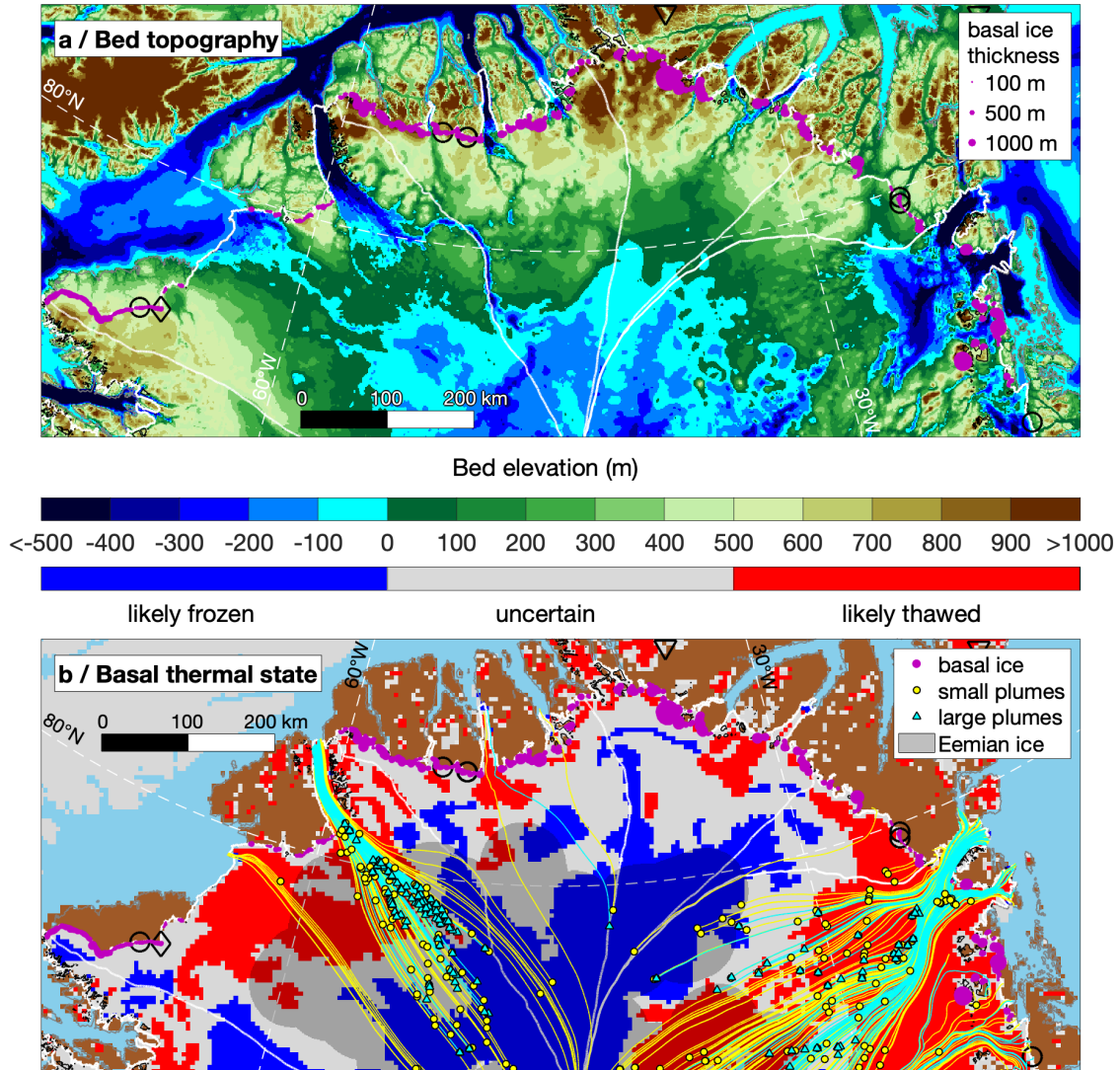
540 The second observation is that – for any given traced segment of the top of the basal ice – this
541 boundary appears to be approximately isochronal, as indicated by where/when it meets the Holocene or
542 LGP ice above it (Fig. 12). This observation suggests that the apparent unconformity at this boundary is
543 due to either an accumulation hiatus, ice erosion or basal freeze-on that occurred at approximately the
544 same time. Further, the age at which this unconformity meets overlying younger ice appears to increase as
545 one moves farther east and north across northern Greenland (Fig. 12). Adjacent to southwestern Inglefield
546 Land, the top of the basal ice appears to intersect early Holocene ice, whereas adjacent to Warming Land
547 or Kronprins Christian Land that intersection appears to occur sometime during the pre-B-A LGP.

548 The third observation is that we mapped basal ice mostly adjacent to local highlands in the bed
549 topography of northern Greenland (Fig. 11a). This observation is unsurprising, because we did not expect
550 to be able to map surface-exposed layering extensively within or alongside most of the heavily sheared,
551 major outlet glaciers that flow through subglacial troughs. However, it could be the most significant of the
552 four, as it establishes a relatively simple spatial relation between the presence of surface-exposed basal
553 ice and higher bed topography. The northern shear margin of Humboldt Glacier (southern Daugaard-
554 Jensen Land) is perhaps the clearest deviation from that pattern, where basal ice is observed immediately
555 adjacent to the subglacial trough that Humboldt Glacier flows through.

556

557

Fig. 11



558

559

560

561

562

563

564

565

566

567

568

569

570

571

572

Fig. 11. Extent of basal ice layer superimposed on (a) BedMachine v3 bed topography (150-m grid; Morlighem and others, 2017) and (b) the likely basal thermal state (5-km grid; MacGregor and others, 2016b). Marker size for basal ice is scaled by its margin-perpendicular horizontal extent (thickness). For panel b, both mapped inland basal ice “plumes” (Leysinger-Vieli and others, 2018) and radiostratigraphy-inferred extent of the top of Eemian ice (115-ka isochrone) in the GrIS interior are overlain (MacGregor and others, 2015); streamlines (solid lines) for basal units calculated using surface-velocity field (Joughin and others, 2017).

Finally, we note that basal ice is observed at the margin of ice-drainage systems that can be either predominantly frozen or thawed (Fig. 11b). Somewhat more basal ice appears present adjacent to predominantly frozen ice-drainage systems in far northern Greenland, but the margin abutting Daugaard-Jensen Land and Kronprins Christian Land is downstream of ice whose bed is likely thawed. Given the preservation of basal ice at these locations, this observation could reflect a limitation of the present basal thermal state synthesis (e.g., Chu and others, 2018). This observation also suggests that cold-based

573 mechanisms likely contribute to the formation of the basal ice outcrops we mapped (Knight, 1997). Very
574 few of the basal ice “plumes” identified by Leysinger Vieli and others (2018) – which they hypothesize are
575 formed by basal freeze-on – are located beneath ice that is presently flowing toward land-terminating
576 margins (Fig. 11b). The radar-inferred distribution of Eemian ice is more widespread than the basal plumes
577 (Fig. 11b), but it is difficult to constrain how thick such ice would be if any of it does indeed emerge at the
578 margin.
579

580 **4. Discussion**

581 **4.1. Implications for *in situ* margin sampling**

582
583
584 A surprising outcome of our study is that – despite its successful subsequent application by later
585 efforts – the visual pattern identified by R02 is only well supported by our comparison of satellite imagery
586 and $\delta^{18}\text{O}$ transects at a pair of adjacent sites in northeastern Greenland (Kronprins Christian Land K/KS,
587 Figs. 3, 4E-H) and our Hiawatha Glacier site (Fig. 6). We find that the sites sampled by R02 constitute a
588 good diversity of expressions of margin layering, but for various reasons the majority of them were
589 suboptimal relative to their stated goal of producing “important and (cheap) supplements to ice core
590 records”, particularly for the northern GrIS. This discovery does not invalidate *in situ* age interpretations at
591 other sites, which often have more complex margin layering, because more detailed sampling
592 commensurate to that layering complexity was performed, along with additional chemical analyses.
593 However, this outcome does warrant additional surface sampling to refine the visual interpretation we
594 applied across the northern GrIS.

595 Two previously unexplored sites of note are those that we identified along the ice margin adjacent
596 to Warming Land, where surface-exposed strata are exceptionally well preserved and likely extend well
597 into the LGP (Fig. 10). These identifications highlight the value of satellite remote sensing for site
598 reconnaissance of ice-margin stratigraphy, because although these two promising sites are 38 km apart,
599 they are both less than 6 km from opportunistic $\delta^{18}\text{O}$ transects collected in 1985 (Table 1; Fig. 4a-d).
600 However, both sites are logistically challenging to reach, as they are more than 500 km from the nearest
601 permanent settlement in Greenland and more than 200 km from Alert, Canada. This situation exemplifies
602 the present balance of risk and reward for accessing surface-exposed paleoclimatically distinct ice in
603 Greenland, i.e., the most promising sites are located in some of the most remote regions of the island.

604 The identification of additional promising sites for margin ice sampling in Greenland is also
605 important for novel measurements of ice properties. While modern measurements of water isotopes and
606 major ion concentrations require only a few milliliters of meltwater (e.g., Bailey and others, 2019),
607 measurements of isotopic or mass concentrations of less common impurities in ice can either require or
608 benefit from significantly larger samples (in some cases >100 kg) that far exceed those of typical ice cores
609 or reasonable allocations thereof (e.g., Steig and others, 1998; Petaev and others, 2013; Buizert and others,
610 2014; Petrenko and others, 2009; Koll and others, 2019). Wide surface exposures of apparently well-
611 behaved layers in the northern GrIS offer the potential for effectively unlimited access to coherent Holocene
612 and pre-Holocene ice at higher temporal resolution than has been possible for some methods that require
613 bulk ice sampling. The northerly reach of these sites suggests they may also represent better proxies for
614 past sea ice extent in the Arctic Ocean than existing deep Greenland ice cores, because surface-exposed
615 ice there likely originates from farther north than those cores (Fig. 10f). However, recent work suggests that
616 ice originating from the GrIS interior is unlikely to be as valuable as that from more coastal Arctic ice caps
617 in constraining past sea ice extent (Rhodes and others, 2018).
618

619 **4.2. Broader applications of mapping margin layering**

620

621 The surface-exposed boundaries that we mapped constitute isochrones (or an unconformity, in the
622 case of the top of the basal ice) that are direct visual analogs to those interfaces regularly mapped by radar
623 sounding in the interior of the ice sheet. Shallow radar sounding of Antarctic blue ice areas has
624 demonstrated correlations between mapped reflections and surface-isotopic profiles (e.g., Winter and
625 others, 2016). However, it is often difficult to trace deep radiostratigraphy within ~100 km of the GrIS margin
626 with the most widely deployed radar sounders (MacGregor and others, 2015; Florentine and others, 2018),
627 and we did not observe coherent surface stratigraphy in our S2 mosaic more than ~100 km inland of the
628 margin because of persistent firn cover in the accumulation zone. Separately, we examined dozens of
629 radargrams intersecting the northern margin that were collected in 2011 and 2014 by Operation IceBridge,
630 and we found that they consistently failed to detect coherent radiostratigraphy there. Thus, the convergence
631 of coherent surface- and radar-mapped layers is rare, but it has been demonstrated at Hiawatha Glacier by
632 Kjær and others (2018) using the latest radar-sounder technology.

633 Just as ice-sheet-wide maps of radiostratigraphy could be used to constrain and initialize ice-flow
634 models (e.g., Clarke and others, 2005; Born, 2017; MacGregor and others, 2016a; Goelzer and others,
635 2018), the surface layers mapped in this study could serve a similar purpose for models that can leverage
636 this information. We are not aware of any large-scale model of the GrIS that is presently equipped to ingest
637 these data directly, although Gilbert and others (2016) did find that a thermomechanical ice-flow model of
638 the Barnes Ice Cap based on Elmer/Ice could successfully reproduce both the borehole-observed depth
639 and the apparent rheological contrast of the Pleistocene–Holocene transition. We recognize that
640 assimilation of these surface strata is unlikely to precede assimilation of radiostratigraphy for several
641 reasons: 1. Observations of the former are not as widespread; 2. The horizontal separation of these
642 boundaries is often significantly less than the spatial resolution of present-generation ice-sheet models; 3.
643 Several additional processes complicate modeling of margin layering, as compared to radiostratigraphy in
644 the accumulation zone (e.g., margin migration, surface melting, seasonally transient supraglacial and
645 subglacial hydrology, formation and advection of basal ice).

646 While this study is the first to map pre-Holocene margin layering across a substantial portion of the
647 GrIS margin, it has several limitations that could be improved upon in future efforts. Foremost is the clear
648 improvement in boundary identification when using finer-resolution WV imagery. The five-to-eight-fold
649 improvement in spatial resolution with only a single bit loss in radiometric resolution (as compared to S2)
650 substantially improves the quality of our pre-Holocene boundary mapping (e.g., Fig. 10). However, the
651 greater data volume of WV imagery and its reduced availability in northern Greenland during our period of
652 interest (late summer) limited the utility thereof to specific narrow regions of interest (Figs. 4, 9, 10). A
653 second limitation is the use of manual boundary tracing, whose trade-offs were discussed in §2.2. A more
654 substantial effort to investigate robust automated identification of surface-exposed layers could result in a
655 more reliable and widespread mapping of GrIS margin stratigraphy, for both Holocene and pre-Holocene
656 layers. Finally, we reiterate that additional *in situ* surface measurements of $\delta^{18}\text{O}$ values and comparison
657 with dated deep ice cores would improve confidence in the boundary ages that we have assumed in this
658 study.

659 Our results also evince a potential terrestrial analog to remote-sensing studies of ice masses
660 elsewhere in the Solar System, in particular the northern polar layered deposits (NPLD) on Mars. There,
661 numerous layers of variable dustiness are also observed by both satellite-based imaging and radar
662 sounding (e.g., Christian and others, 2013; Lalic and others, 2019). These layers outcrop along the
663 margins of the NPLD and have been linked statistically to nearby radiostratigraphy, but no *in situ* sampling
664 has yet been performed, despite its potential value in deciphering recent martian climate history. The
665 northern GrIS is remote – but less so than Mars – and the warmer, faster GrIS is an imperfect analog to the
666 colder, near-static NPLD. However, future exploration of the margin of the northern GrIS could better
667 constrain the geometric and englacial conditions that result in detectable surface and englacial stratigraphy.
668 Such data could inform instrument requirements for future interplanetary missions to study the martian
669 climate history recorded by the NPLD (Smith and others, 2020b).

670
671
672
673
674
675
676
677
678
679
680
681
682
683
684
685
686
687
688
689
690
691
692
693
694
695
696
697
698
699
700
701
702
703
704
705
706
707
708
709
710
711
712
713
714
715
716
717

4.3. The significance of northern Greenland's basal ice

An outstanding question raised by our examination of the northern margin of the GrIS is the significance of the widespread basal ice whose upper boundary we mapped (Fig. 11). Margin-exposed basal ice is famously complex, and our remote observations and limited *in situ* sampling cannot substitute for more detailed direct investigation thereof, so we cannot yet reliably interpret its apparent composition or formation mechanism from space (e.g., Knight, 1997; Larsen and others, 2010). While our *in situ* measurements indicate that unit is indeed basal ice (Fig. 6), it is not yet certain that the unit we mapped can strictly be considered basal ice, as it is not consistently sediment-rich, nor have we demonstrated that all this ice has flowed within meters of the bed. Regardless, in the basal ice taxonomy put forth by Knight (1997), the most plausible interpretation is that we have mapped the top of dispersed facies, i.e., “ice that has been so affected by metamorphic processes close to the bed that it displays the features of neither meteoric glacier ice nor basally frozen ice.” Such ice is expected to have a lower debris content than the dark brown ice-cemented debris layers sometimes observed at base of Greenlandic glaciers (e.g., Larsen and others, 2010). This interpretation is consistent with the widespread geographic distribution of the unit (Fig. 11), but not with the occasional observations of distinct strata apparent in WV imagery (Figs. 9A,B, 10; Figs. 13, 14). However, Knight (1997) acknowledge that a continuum of basal ice facies is sometimes observed, and that stratified basal ice is more commonly observed below dispersed facies, which is roughly consistent with our observations and others in Greenland (e.g., Larsen and others, 2010).

Basal ice formation is generally attributed to cold-based glacier flow. While our basal ice distribution is somewhat consistent with being the downstream product of cold-based ice flow, it is not conclusively so, and the basal thermal state could easily have varied in the past (Fig. 11b). However, geologic observations of the deglaciated forelands across much of northern Greenland also suggest long periods of minimally erosive, cold-based glacier conditions, even during glacial periods with greater ice extent (e.g., Pedersen and others, 2019). A simple synthesis of those observations and ours could be that – outside of the tributary regions for major outlet glaciers and other anomalous subglacial structures – a frozen basal thermal state has persisted beneath the northern GrIS during most of the LGP and the Holocene. Otherwise, widespread pre-Holocene and basal ice is less likely to have survived and the deglaciated landscape would indicate greater long-term erosion rates. Absent additional direct observations of the ice unit whose top we mapped, the above arguments are speculative, but they can plausibly explain several of our observations and warrant further consideration – potentially as targets for studies of the past flow of the GrIS.

5. Conclusions

We synthesized existing observations of surface stratigraphy along the margin of the GrIS with a new satellite-based mapping of key boundaries in that stratigraphy along its northern margin. Effectively, we leveraged a decades-old insight from field observations into the first large-scale evaluation of the age of the northern margin of the GrIS. We described both typical and anomalous margin exposures across northern Greenland and identified promising sites for future recovery of paleoclimatically valuable ice, of which two sites adjacent to Warming Land hold the most promise. We find that large exposures of basal ice are more common across the margin of the northern GrIS than previously known, but that the significance of these exposures remains unclear. We speculate that they indicate long-term persistence of cold-based conditions beneath most of the northern GrIS.

This study was enabled by access to large volumes of satellite imagery that could be processed efficiently and remotely into a mosaic of direct scientific value. Our approach favored simplicity, speed and reliability in mosaic generation and boundary tracing over methodological sophistication, and as a result we were able to explore a large portion of the GrIS efficiently. We suggest that future remote-sensing studies

718 of the GrlS and other ice masses considering similarly large scales use these resources to accelerate
719 studies of difficult-to-access regions.

720

721 **Supplementary material**

722

723 The supplementary material for this article can be found at [X](#). The JavaScript code used to generate
724 the filtered August 2019 S2 mosaic within Google Earth Engine is provided in Supplementary File 1 as a
725 plain text file. The layer boundaries we traced are available as ESRI shapefiles in Supplementary File 2 as
726 a zipped archive, for which the projection used is EPSG:3413 (NSIDC See Ice Polar Stereographic North).
727 Supplementary Files 3, 4 and 5 are video animations whose snapshots are shown in Figures 12, 13 and
728 14, respectively (Appendix A) and have a standard 1080p resolution in MPEG-4 format. The frame rate of
729 Supplementary File 3 is 2 fps for easy pausing between scenes and boundary overlays, whereas for
730 Supplementary Files 4 and 5, it is 30 fps.

731

732 **Data availability**

733

734 Some of the satellite data presented in this article are freely available and archived online. In
735 particular, the S2 mosaic is presently available as a cloud-served basemap within the ITS_LIVE QGIS
736 project file for Greenland (Gardner and others, 2020). The source URL for that mosaic can be added as a
737 raster layer within any QGIS project. The MATLAB script used to process the data used in this study and
738 to generate the figures is freely available from the corresponding author (JAM) upon request.

739

740 **Acknowledgments**

741

742 We thank the Goddard Fellows Innovation Challenge for supporting JAM's fieldwork and data
743 analysis. We thank ESA/Copernicus for unrestricted access to the S2 imagery used in this study and
744 Google Earth Engine for free access to their cloud computing resources. We thank the Polar Geospatial
745 Center (PGC) and DigitalGlobe Inc. for access to WV imagery, and the PGC for ArcticDEM. We recognize
746 the pioneering efforts of the late Niels Reeh, whose work provided both the inspiration and basis for this
747 study. We thank Hans Oerter for providing a digital copy of $\delta^{18}\text{O}$ data collected several decades ago and
748 permission to use his photograph, and Niels "Oscar" Henriksen for improved coordinates of the four
749 Warming Land sites and valuable discussions concerning sampling methods there. We thank Pierre Beck,
750 Anders Bjørk, Ludovic Brucker, Jessy Jenkins, Hans-Peter Marshall, Jérémie Mougnot and Lincoln Pitcher
751 for equipment loans and fieldwork assistance, and John Sonntag for permission to use his photograph.
752 Finally, we thank Chief Editor Hester Jiskoot, Scientific Editor Beatá Csathó and two anonymous reviewers
753 for their constructive reviews of the manuscript.

754

755 **Author contributions**

756

757 All authors contributed to both the data interpretation and writing. JAM conceived the study and led
758 the fieldwork, data analysis, interpretation and writing. MAF led the mosaic generation, WTC led the data
759 archaeology, NKL and KKK led the interpretation of the basal ice mapping, and JMW led the laboratory
760 analysis.

761

762 **References**

763

- 764 **Aciego SM, Cuffey KM, Kavanaugh JL, Morse DL and Severinghaus JP** (2007) Pleistocene ice and
765 paleo-strain rates at Taylor Glacier, Antarctica, *Quaternary Research* **68**(3), 303–313,
766 doi:10.106/j.yqres.2007.07.013
- 767 **Bailey H, Klein ES and Welker JM** (2019) Synoptic and mesoscale mechanisms drive winter precipitation
768 $\delta^{18}\text{O}/\delta^2\text{H}$ in south-central Alaska, *Journal of Geophysical Research Atmospheres* **124**, 4252–4266,
769 doi:10.1029/2018JD030050
- 770 **Bøggild CE, Oerter H and Tukiainen T** (1996), Increased ablation of Wisconsin ice in eastern north
771 Greenland: observations and modelling, *Annals of Glaciology* **23**, 144–148,
772 doi:10.3189/S0260305500013367
- 773 **Bøggild CE, Brandt, RE, Brown, KJ and Warren SG** (2010) The ablation zone in northeast Greenland:
774 ice types, albedos and impurities, *Journal of Glaciology* **56**(195), 101–113,
775 doi:10.3189/002214310791190776
- 776 **Born A** (2017) Tracer transport in an isochronal ice-sheet model, *Journal of Glaciology* **63**(237), 22–38,
777 doi:10.1017/jog.2016.111
- 778 **Buizert C and 10 others** (2014) Radiometric ^{81}Kr dating identifies 120,000-year-old ice at Taylor Glacier,
779 Antarctica, *Proceedings of the National Academy of Sciences* **111**(19), 6876–6881,
780 doi:10.1073/pnas.1320329111
- 781 **Christian S, Holt JW, Byrne S and Fishbaugh KE** (2013) Integrating radar stratigraphy with high
782 resolution visible stratigraphy of the north polar layered deposits, Mars, *Icarus* **226**(2), 1241–1251,
783 doi:10.1016/j.icarus.2013.07.003
- 784 **Chu W, Schroeder DM, Seroussi H, Creyts TT and Bell RE** (2018), Complex Basal Thermal Transition
785 Near the Onset of Petermann Glacier, Greenland, *Journal of Geophysical Research Earth Surface* **123**,
786 doi:10.1029/2017JF004561
- 787 **Clarke GKC, Lhomme N and Marshall SJ** (2005) Tracer transport in the Greenland ice sheet: three-
788 dimensional isotopic stratigraphy, *Quaternary Science Reviews* **24**(1-2), 155–171,
789 doi:10.1016/j.quascirev.2004.08.021
- 790 **Craig H** (1961) Isotopic Variations in Meteoric Waters, *Science* **133**(346), 1702–1703
- 791 **Fahnestock MA, Bindschadler RA, Kwok R and Jezek KC** (1993) Greenland ice sheet surface properties
792 and ice dynamics from ERS-1 SAR imagery, *Science* **262**, 1530–1534
- 793 **Fahnestock MA, Scambos TA, Moon T, Gardner AS, Haran TM and Klinger M** (2016) Rapid large-area
794 mapping of ice flow using Landsat 8, *Remote Sensing of the Environment* **185**(C), 84–94,
795 doi:10.1016/j.rse.2015.11.023
- 796 **Florentine C, Harper JT, Johnson JV and Meierbachtol T** (2018) Radiostratigraphy reflects the present-
797 day, internal ice flow field in the ablation zone of western Greenland, *Frontiers in Earth Science* **6**,
798 1728–11, doi:10.3389/feart.2018.00044
- 799 **Gardner AS, Fahnestock MA and Scambos TA** (2020), ITS_LIVE Regional Glacier and Ice Sheet Surface
800 Velocities. Data archived at National Snow and Ice Data Center; doi:10.5067/6II6VW8LLWJ7
- 801 **Gilbert A, Flowers GE, Miller GH, Rabus BT, Van Wychen W, Gardner AS and Copland L** (2016)
802 Sensitivity of Barnes Ice Cap, Baffin Island, Canada, to climate state and internal dynamics, *Journal of*
803 *Geophysical Research Earth Surface* **121**, doi: 10.1002/2016JF003839
- 804 **Goelzer H and 30 others** (2018) Design and results of the ice sheet model initialisation initMIP-Greenland:
805 an ISMIP6 intercomparison, *The Cryosphere* **12**(4), 1433–1460, doi:10.5194/tc-12-1433-2018
- 806 **Gorelick N, Hancher M, Dixon M, Ilyushchenko S, Thau D and Moore R** (2017) Google Earth Engine:
807 Planetary-scale geospatial analysis for everyone, *Remote Sensing of the Environment* **202**, 18–27,
808 doi:10.1016/j.rse.2017.06.031
- 809 **Hooke RL** (1976) Pleistocene ice at the base of the Barnes Ice Cap, Baffin Island, N.W.T., Canada, *Journal*
810 *of Glaciology* **17**(75), 49–59, doi:10.3189/S0022143000030719
- 811 **Hooke R** (2005) Chapter 13: Finite strain and the origin of foliation, in *Principles of Glacier Mechanics*,
812 Cambridge University Press. ISBN 0-521-83609-3

- 813 **Howat I** (2017) MEaSURES Greenland Ice Mapping Project (GIMP) Land Ice and Ocean Classification
814 Mask, Version 1, NASA National Snow and Ice Data Center Distributed Active Archive Center.
815 doi:10.5067/B8X58MQBFUPA
- 816 **Howat IM, Negrete A and Smith BE** (2014) The Greenland Ice Mapping Project (GIMP) land classification
817 and surface elevation data sets, *The Cryosphere* **8**(4), 1509–1518, doi:10.5194/tc-8-1509-2014
- 818 **Hudleston PJ** (2015), Structures and fabrics in glacial ice: A review, *Journal of Structural Geology* **81**(C),
819 1–27, doi:10.1016/j.jsg.2015.09.003.
- 820 **Joughin IR, Smith BE and Howat IM** (2017) A complete map of Greenland ice velocity derived from
821 satellite data collected over 20 years, *Journal of Glaciology* **64**(243), 1–11, doi:10.1017/jog.2017.73.
- 822 **Kjær KH and 21 others** (2018) A large impact crater beneath Hiawatha Glacier in northwest Greenland,
823 *Science Advances* **4**(11), doi:10.1126/sciadv.aar8173
- 824 **Kjeldsen KK and 15 others** (2015), Spatial and temporal distribution of mass loss from the Greenland Ice
825 Sheet since AD 1900, *Nature* **528**(7582), 396–400, doi:10.1038/nature16183
- 826 **Koll, D and 6 others** (2019) Interstellar ⁶⁰Fe in Antarctica, *Physical Review Letters* **123**(7), 072701,
827 doi:10.1103/PhysRevLett.123.072701
- 828 **Knight PG** (1997), The basal ice layer of glaciers and ice sheets, *Quaternary Science Reviews* **16**, 975–
829 993 doi:10.1016/s0277-3791(97)00033-4
- 830 **Kurbatov AV and 22 others** (2010) Discovery of a nanodiamond-rich layer in the Greenland ice sheet,
831 *Journal of Glaciology* **56**(199), 747–757, doi:10.3189/002214310794457191
- 832 **Lalich DE, Holt JW and Smith IB** (2019) Radar reflectivity as a proxy for the dust content of individual
833 layers in the Martian north polar layered deposits, *Journal of Geophysical Research Planets* **124**(7),
834 doi:10.1029/2018JE005787
- 835 **Larsen NK, Kronborg C, Yde JC and Knudsen NT** (2010) Debris entrainment by basal freeze-on and
836 thrusting during the 1995-1998 surge of Kuannersuit Glacier on Disko Island, west Greenland, *Earth*
837 *Surface Processes and Landforms* **16**(B4), 561–574, doi:10.1002/esp.1945
- 838 **Leysinger Vielí GJMC, Martin C, Hindmarsh RCA and Lüthi MP** (2018) Basal freeze-on generates
839 complex ice-sheet stratigraphy, *Nature Communications* **9**(1), 1–13, doi:10.1038/s41467-018-07083-3
- 840 **MacGregor JA and 9 others** (2015) Radiostratigraphy and age structure of the Greenland Ice Sheet,
841 *Journal of Geophysical Research Earth Surface* **120**(2), 212–241, doi:10.1002/2014JF003215
- 842 **MacGregor JA and 6 others** (2016a) Holocene deceleration of the Greenland Ice Sheet, *Science*
843 **351**(6273), 590–593, doi:10.1126/science.aab1702
- 844 **MacGregor JA and 11 others** (2016b) A synthesis of the basal thermal state of the Greenland Ice Sheet,
845 *Journal of Geophysical Research Earth Surface* **121**(7), 1328–1350, doi:10.1002/2015JF003803
- 846 **McGrath D, Colgan WT, Bayou N, Muto A and Steffen K** (2013) Recent warming at Summit, Greenland:
847 Global context and implications, *Geophysical Research Letters* **40**(10), 2091–2096,
848 doi:10.1002/grl.50456
- 849 **Morlighem M and 31 others** (2017) BedMachine v3: Complete Bed Topography and Ocean Bathymetry
850 Mapping of Greenland From Multibeam Echo Sounding Combined With Mass Conservation,
851 *Geophysical Research Letters* **44**, 11,051–11,061, doi:10.1002/2017GL074954
- 852 **Mouginot J, Bjørk AA, Millan R, Scheuchl B and Rignot EJ** (2018) Insights on the surge behavior of
853 Storstrømmen and L. Bistrup Brae, Northeast Greenland, over the last century, *Geophysical Research*
854 *Letters* **45**, doi:10.1029/2018GL079052
- 855 **Noël B, van de Berg WJ, Lhermitte S and van den Broeke MR** (2019) Rapid ablation zone expansion
856 amplifies north Greenland mass loss, *Science Advances* **5**(9), doi:10.1126/sciadv.aaw0123
- 857 **Pedersen VK, Larsen NK and Egholm DL** (2019) The timing of fjord formation and early glaciations in
858 North and Northeast Greenland, *Geology* **47**(7), 682–686, doi:10.1130/G46064.1.
- 859 **Petaev MI, Huang S, Jacobsen SB and Zindler A** (2013) Large Pt anomaly in the Greenland ice core
860 points to a cataclysm at the onset of Younger Dryas, *Proceedings of the National Academy of Sciences*
861 **110**(32), 12917–12920, doi:10.1073/pnas.1303924110

- 862 **Petrenko VV, Severinghaus JP, Brook EJ, Reeh N and Schaefer H** (2006) Gas records from the West
863 Greenland ice margin covering the Last Glacial Termination: a horizontal ice core, *Quaternary Science*
864 *Reviews* **25**(9-10), 865–875, doi:10.1016/j.quascirev.2005.09.005
- 865 **Petrenko VV and 11 others** (2009) ¹⁴CH₄ measurements in Greenland ice: investigating last glacial
866 termination CH₄ sources, *Science* **324**, 506–508, doi:10.1126/science.1168909
- 867 **Porter C and 28 others** (2018) ArcticDEM v7, Harvard Dataverse, v1, doi:10.7910/DVN/OHHUKH
- 868 **Post A** (1972) Periodic surge origin of folded medial moraines on Bering Piedmont Glacier, Alaska, *Journal*
869 *of Glaciology* **11**(62), 219–226, doi:10.3189/S0022143000022218
- 870 **Putman AL, Fiorella RP, Bowen GJ and Cai X** (2019) A global perspective on local meteoric water lines:
871 Meta-analytic insight into fundamental controls and practical constraints, *Water Resources Research*
872 **55**(8), 6896–6910, doi:10.1029/2019WR025181
- 873 **Rasmussen, SO and 15 others** (2006), A new Greenland ice core chronology for the last glacial
874 termination, *Journal of Geophysical Research* **111**(D6), D06102, doi:10.1029/2005JD006079
- 875 **Reeh N, Oerter H and Thomsen HH** (2002) Comparison between Greenland ice-margin and ice-core
876 oxygen-18 records, *Annals of Glaciology* **35**, 136–144
- 877 **Rhodes RH, Yang X and Wolff EW** (2018) Sea Ice Versus Storms: What Controls Sea Salt in Arctic Ice
878 Cores? *Geophysical Research Letters* **45**(11), 5572–5580, doi:10.1029/2018GL077403
- 879 **Risbo T and Pedersen H** (1994) Kap York - meteoritekspeditionen, In *Carlsbergfondet*
880 *Frederiksborgmuseet Ny Carlsbergfondet Ærsskrift*. Copenhagen, RHODOS Internationalt Forlag for
881 Videnskab og Kunst, 38–45
- 882 **Ruth U, Wagenbach D, Steffensen JP and Bigler M** (2003) Continuous record of microparticle
883 concentration and size distribution in the central Greenland NGRIP ice core during the last glacial
884 period, *Journal of Geophysical Research* **108**(D3), 4098, doi:10.1029/2002JD002376
- 885 **Ryan JC and 7 others** (2018), Dark zone of the Greenland Ice Sheet controlled by distributed biologically-
886 active impurities, *Nature Communications* **9**, doi:10.1038/s41467-018-03353-2
- 887 **Schaefer H and 6 others** (2009) Ice stratigraphy at the Pâkitsoq ice margin, West Greenland, derived from
888 gas records, *Journal of Glaciology* **55**(191), 411–421, doi:10.3189/002214309788816704
- 889 **Schäfer JM and 6 others** (2000) The oldest ice on Earth in Beacon Valley, Antarctica: new evidence from
890 surface exposure dating, *Earth and Planetary Science Letters* **179**(1), 91–99, doi:10.1016/S0012-
891 821X(00)00095-9
- 892 **Sinisalo A and Moore JC** (2010) Antarctic blue ice areas - towards extracting palaeoclimate information,
893 *Antarctic Science* **22**(2), 99–115, doi:10.017/S0954102009990691
- 894 **Smith BE and 14 others** (2020a), Pervasive ice sheet mass loss reflects competing ocean and atmosphere
895 processes, *Science* **368**(6946), 1239–1242, doi:10.1126/science.aaz5845
- 896 **Smith IB and 37 others** (2020b) The Holy Grail: A road map for unlocking the climate record stored within
897 Mars' polar layered deposits, *Planetary and Space Science* **184**, 104841,
898 doi:10.1016/j.pss.2020.104841
- 899 **Steig EJ, Morse DL, Waddington ED and Polissar PJ** (1998) Using the sunspot cycle to date ice cores,
900 *Geophysical Research Letters* **25**(2), 163–166, doi:10.1029/97GL03566
- 901 **Tedesco M and Fettweis X** (2020) Unprecedented atmospheric conditions (1948–2019) drive the 2019
902 exceptional melting season over the Greenland ice sheet, *The Cryosphere* **14**, 1209–1223,
903 doi:10.5194/tc-2019-254
- 904 **Wientjes IGM, van de Wal RSW, Schwikowski M, Zapf A, Fahrni S and Wacker L** (2012) Carbonaceous
905 particles reveal that Late Holocene dust causes the dark region in the western ablation zone of the
906 Greenland ice sheet, *Journal of Glaciology* **58**(210), 787–794, doi:10.3189/2012JoG11J165
- 907 **Winter, K and 10 others** (2016) Assessing the continuity of the blue ice climate record at Patriot Hills,
908 Horseshoe Valley, West Antarctica, *Geophysical Research Letters* **43**(5), 2019–2026,
909 doi:10.1002/2015GL066476

910 **Yan Y and 10 others** (2019) Two-million-year-old snapshots of atmospheric gases from Antarctic ice,
911 *Nature* **574**, 663–666, doi:10.1038/s41586-019-1692-3

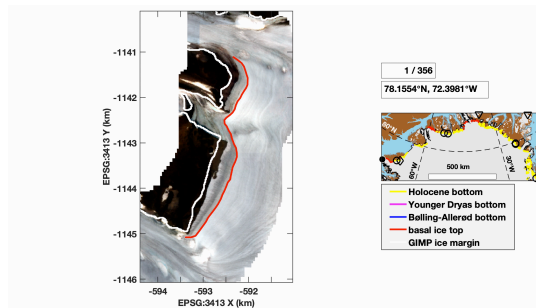
912 **Yang K, Smith LC, Sole AJ, Livingstone SJ, Cheng X, Chen Z and Li M** (2019) Supraglacial rivers on
913 the northwest Greenland Ice Sheet, Devon Ice Cap, and Barnes Ice Cap mapped using Sentinel-2
914 imagery, *International Journal of Applied Earth Observation and Geoinformation* **78**, 1–13,
915 doi:10.1016/j.jag.2019.01.008

916 **Zwally HJ, Giovinetto MB, Beckley MA and Saba JL** (2012) Antarctic and Greenland drainage systems,
917 http://icesat4.gsfc.nasa.gov/cryo_data/ant_grn_drainage_systems.php
918

919 APPENDIX A – ANIMATIONS

920
921

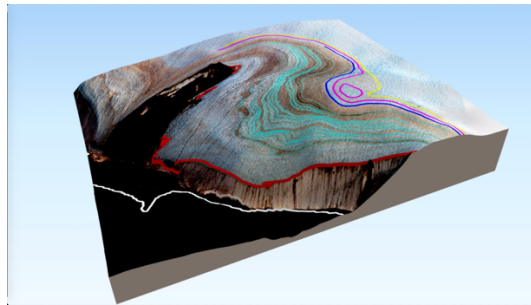
Fig. 12



922
923 **Fig. 12.** Snapshot of Supplementary File 3. All traced boundary segments shown sequentially, clockwise
924 about northern Greenland. A sub-scene of the S2 mosaic is generated for each digitized point with a 1-km
925 buffer, then contrast-stretched to emphasize margin stratigraphy. Note that the scale for each frame varies
926 depending on segment length, but that it is typically larger than that at which we traced boundaries in the
927 imagery (1:10,000). Contains Copernicus Sentinel-2 2019 data, processed by ESA.

928
929

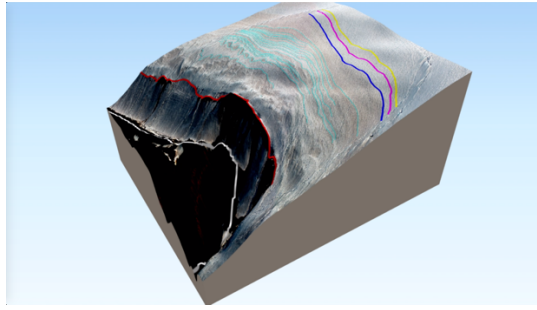
Fig. 13



930
931 **Fig. 13.** Snapshot of Supplementary File 4. A rotation about a three-dimensional representation of Fig. 10a,
932 i.e., the same WV subscene draped over ArcticDEM. Vertical exaggeration is 5x. WV imagery is copyright
933 2020 DigitalGlobe Inc.
934

935

Fig. 14



936

937

938

Fig. 14. Snapshot of Supplementary File 5. Same as Fig. 13 but showing same region as Fig. 10b. WV imagery is copyright 2020 DigitalGlobe Inc.